

Investigation of Ultrafast Carrier Dynamics in InGaN/GaN-Based Nanostructures Using Femtosecond Pump–Probe Absorption Spectroscopy

Tarni Aggarwal, Ankit Udai, Debashree Banerjee, Vikas Pendem, Shonal Chouksey, Pratim Saha, Sandeep Sankaranarayanan, Swaroop Ganguly, Pallab Bhattacharya, and Dipankar Saha*

GaN-based optoelectronic devices including light-emitting diodes and lasers realized with quantum-confined nanostructures, revolutionized the solid-state lighting. Excited-state ultrafast nonlinear dynamics of these nanostructures are crucial in determining the device performance in terms of luminescence efficacy, emission spectra, wall-plug efficiency, turn-on delay, lasing threshold current, and modulation bandwidth. Therefore, understanding the carrier and photon dynamics of these nanostructures is of utmost importance. A comparative investigation of ultrafast nonlinear carrier-photon dynamics of 2D, 1D, and 0D InGaN/GaN nanostructures is carried out. Femtosecond pump–probe absorption spectroscopy is used uniformly herein to obtain the wavelength-dependent ultrafast kinetics of these nanostructures, with a temporal resolution of ≈ 50 fs. Carrier thermalization and relaxation processes of all the samples are studied both experimentally and theoretically. Distinguished phenomena, such as fast carrier trapping and subsequent detrapping of the carriers from sub-bandgap defect states are observed. Real-time monitoring of quantum confined Stark effect, enhanced radiative recombination, and diffusion-limited carrier kinetics are manifested. Carrier capture and recombination time constants are calculated theoretically, considering quantum properties. Theoretical values are in good agreement with the experimental observations. In addition, transient absorption spectroscopy is used to investigate and decouple the surface and the bulk properties of GaN surfaces.

1. Introduction to InGaN/GaN Quantum-Confined Heterostructures


III–V compound semiconductors laid the foundation for optoelectronic devices and solid-state lighting with wavelengths ranging from infrared to ultraviolet regions. Infrared to green light-emitting diodes (LEDs) were invented in the early 1960s.^[1–3] However, blue LEDs took another three decades to get established, considering the challenges in defect-free high-quality growth,^[4–6] and controlled p-doping of wide-bandgap semiconductors.^[7–10] The success of blue LEDs was accomplished by the development of gallium-nitride (GaN) alloyed with indium and aluminum in the late 1980s.^[11,12] GaN and related materials have a wurtzite crystal structure and direct bandgap, making them ideal for bright LEDs and laser diodes (LDs). In order to move the emission wavelength to the visible range (2–3.4 eV), InN is alloyed with GaN.^[13,14] Advancement in GaN-based LEDs revolutionized the white broadband lighting when laminated with yellow phosphorous coating. Nakamura et al. developed the first high-quality InGaN back in 1992,

which paved the way for III-nitride blue and green LEDs/LDs.^[15] In 1995–1996, Nakamura made true blue LEDs possible by developing recombination regions with InGaN.^[16]

III-nitride devices acquire a wide area of applications due to their wavelength tunability by varying the alloy composition of In and Al in InGaN and AlGaIn, respectively.^[17,18] Moreover, an additional degree of freedom can be achieved using quantum-confined nanostructures. Emission wavelength and surface/interface material properties can be altered by reducing the dimensionality/size of the devices.^[19–21] quantum well (QW; 2D),^[22–24] vertical/lateral nanowires (1D),^[25–29] and quantum dots (QDs; 0D)^[30–33] are among the most important quantum-confined nanostructures used in the active regions of modern optoelectronic devices including LEDs, lasers, photo-detectors, and solar cells. Improved internal quantum efficiency,^[34–36] large surface-to-volume ratio,^[37] low power

T. Aggarwal, A. Udai, D. Banerjee, V. Pendem, S. Chouksey, P. Saha, S. Sankaranarayanan, S. Ganguly, D. Saha
Applied Quantum Mechanics Laboratory
Department of Electrical Engineering
Indian Institute of Technology Bombay
Powai, Mumbai 400076, India
E-mail: dipankarsaha@iitb.ac.in

P. Bhattacharya
Department of Electrical Engineering and Computer Science
University of Michigan
Ann Arbor, MI 48109-2122, USA

 The ORCID identification number(s) for the author(s) of this article can be found under <https://doi.org/10.1002/pssb.202100223>.

DOI: 10.1002/pssb.202100223

consumption,^[38–40] strain-free and defect-free growth mechanism,^[41,42] and larger electron-hole wavefunction overlap due to higher confinement are some of the major advantages of these nanostructures.^[43]

GaN-based quantum-confined light emitters have a variety of applications, including high-resolution printing, display technology, high-speed data processing, interconnects, and optical communication.^[44,45] For high-speed applications, it is crucial to understand the linear and non-linear dynamics of these devices.^[31,46,47] Carrier dynamics enable us to temporally resolve the various scattering and recombination pathways during thermalization and relaxation of the photoexcited carriers. The time constants for high energy carrier-thermalization and recombination primarily determine the maximum achievable internal quantum efficiency,^[48–50] wall-plug efficiency, modulation bandwidth,^[51,52] threshold current density, and turn-on delay.^[30,53,54] Coupled carrier and photon dynamics of these devices are on the time scale of femtoseconds to nanoseconds.^[30] Therefore, fundamental phenomena in such short time scales are of crucial importance. Femtosecond pump–probe absorption spectroscopy on nanostructures is one of the most powerful tools to determine such ultrafast carrier dynamics, which is the central theme of this work.

2. Typical Nonlinear Carrier and Photon Dynamics in Semiconductors

The salient features of nonlinear dynamics in semiconductors under optical excitation are discussed in this section.^[55,56]

Figure 1 shows the excess carrier relaxation processes and the time scale over which each such process occurs. Before excitation ($t = 0^-$), the system remains in thermal equilibrium, as shown in **Figure 1a**. Carrier distribution is also shown therein. At $t = 0$, a high-intensity pump–pulse with energy greater than the semiconductor bandgap ($\hbar\omega_{\text{ex}}$) excites the sample and generates excess electron–hole pairs, shown as process P1 in **Figure 1b**. The excited carrier density is proportional to the density of states (DOS) of the semiconductor and incident photon density. Excited-state (non-thermal) distribution of the hot carriers is depicted with a sharp peak at high energy ($E_2 - E_1 = \hbar\omega_{\text{ex}}$),

as shown in **Figure 1b**. The excited carriers at high energy are then thermalized to the respective band-edges via longitudinal optical phonon emission of energy $\hbar\omega_{\text{LO}}$, shown as process P2 in **Figure 1c**. Carrier thermalization is a relatively fast process, typically in the range of 10 fs to 1 ps. Once excited carriers attain thermal equilibrium with the lattice temperature, decay processes prevail to bring the system to equilibrium. **Figure 1d** shows the nonradiative Auger recombination process (P3), which dominates at high carrier density over a time scale of 1–10 ps. Semiconductors typically have some shallow or deep sub-bandgap defect states. Carriers from the band-edge quickly get trapped into these states within a short span of 10–100 ps, as shown in **Figure 1e**. More the number of traps faster is the trapping rate (discussed later in detail). Further decay of excess carriers take place through band-to-band (BTB) or excitonic radiative recombination (process P5), and nonradiative Shockley–Read–Hall (SRH) recombination (process P6), shown in **Figure 1f,g**, respectively. In addition to the excitonic or BTB radiative recombination, the donor/acceptor interface of optoelectronic-diodes can also experience recombination through geminate pairs^[57] (bound electron–hole pairs at the donor/acceptor interface). The radiative recombination lifetime of typical compound semiconductors is in the range of 0.1–100 ns, whereas SRH recombination takes microseconds.^[32] Femtosecond pump–probe spectroscopy is among the best-suited tools to precisely study these nonlinear ultrafast carrier kinetics, as discussed in the following section.

3. Femtosecond Pump–Probe Absorption Spectroscopy

Advancements in ultrashort tuneable laser pulses in the early 1990s have taken time-resolved optical spectroscopies to new heights. Nonlinear optical measurements are possible with time resolution in the range of femtoseconds (sub 50 fs) using precisely timed and tuned multiple laser pulses. This allows us to probe the nonlinear ultrafast dynamics of an optically excited system.^[58–60] It facilitates the measurement of photoinduced excited-state absorption (ESA) and transmission energies

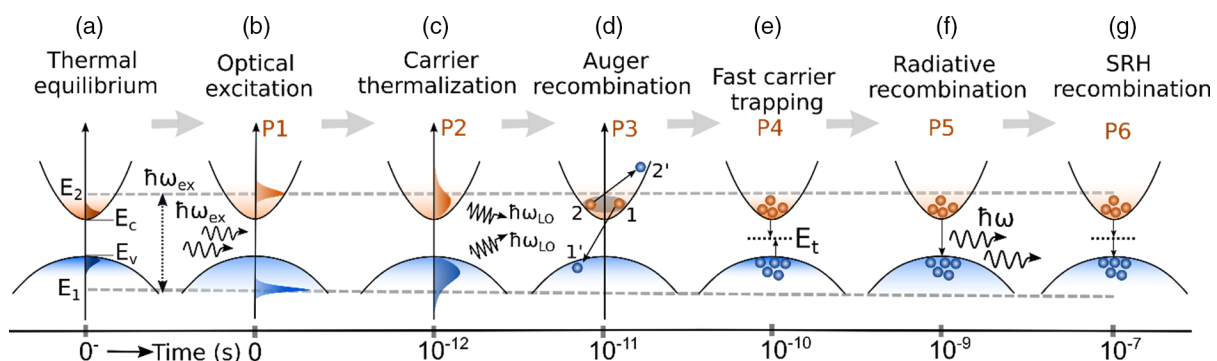


Figure 1. Schematics of excited-state carrier thermalization and relaxation processes in bulk semiconductor along with the associated time scale of each process (P1–P6). a) Electron distribution at thermal equilibrium; b) excess carrier distribution under optical excitation with photon energy $\hbar\omega_{\text{ex}}$ at $t = 0$ (process P1); c) carrier thermalization via optical phonon emission of energy $\hbar\omega_{\text{LO}}$, at $t \approx 10\text{--}1000$ fs (process P2); d) nonradiative Auger recombination, at $t \approx 1\text{--}10$ ps (process P3, dominates only at high carrier density); e) fast carrier trapping in sub-bandgap states, at $t \approx 10\text{--}100$ ps (process P4); f) radiative recombination by emitting photons of energy $\hbar\omega$, at $t \approx 0.1\text{--}100$ ns (process P5); g) nonradiative defect-assisted SRH recombination, at $t \approx 0.1\text{--}1$ μs (process P6).

of the carriers or molecules, along with their associated lifetimes.^[19,55,61] The basic concept of pump–probe spectroscopy is schematically shown in **Figure 2a**. A high-intensity ultrafast (temporal width ≤ 50 fs) pulsed laser beam, called pump, is used to excite the sample. Pump-induced excited carriers are monitored using a weak broadband pulse (called a probe), derived from the same laser source as the pump. Change in the absorption of the probe pulse is measured as a function of probe wavelength, pump wavelength, and relative delay between pump and probe pulses. The energy of the pump–pulse is usually greater than the bandgap of the sample.

Pump–probe technique is successfully utilized in determining the time scale of excited-state dynamics, and energy transfer mechanisms in singlet and triplet states.^[19,62] It has found wide applications in the area of photochemical science, signaling of the human retina, the study of photophysics in dye molecules, exciton (electron–hole pair in semiconductors) dynamics, carrier-phonon scatterings rates, and optimizing the performance of optoelectronic devices.^[56,58,60,61,63–67] Although the energy gaining mechanism in photoexcitation and through applied electric fields are different for electrons, they lose energy to the lattice by the same process in both cases. Therefore, information obtained from pump–probe spectroscopy can also be utilized in understanding high-field carrier transport in electronic devices.

Unlike fluorescence spectroscopies, which detect emitted photons through BTB recombination, pump–probe absorption spectroscopy probes the excited carriers in the system (through differential absorption measurement) to determine the effective carrier lifetime for both radiative and nonradiative recombination processes. Differential absorption ($\Delta\alpha$) is the change in absorbance for the probe photons, with and without pump excitation at various delay time t (time elapsed after pump induced excitation) and probe wavelength (λ):

$$\Delta\alpha(t, \lambda) = \alpha_w(t, \lambda) - \alpha_{w_0}(t, \lambda) \quad (1)$$

Here, α_w and α_{w_0} are the absorbance with and without pump-induced excitation of the sample, respectively. The detector measures photoinduced change in the probe intensity, which is related to differential absorption as

$$\Delta\alpha(t, \lambda) = -\log\left(\frac{I_w(t, \lambda)}{I_{w_0}(\lambda)}\right) = -\log\left(1 + \frac{\Delta I(t, \lambda)}{I_{w_0}(\lambda)}\right) \quad (2)$$

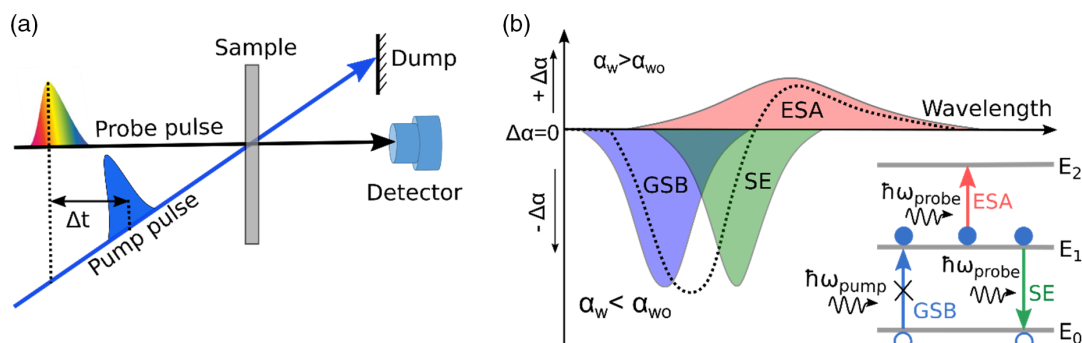


Figure 2. a) Schematic of pump–probe spectroscopy, Δt is the time delay between pump and probe pulse. Pump pulse excites the sample and after some delay probe pulse passes through the sample and monitor the pump-induced changes; b) schematic of differential absorption spectra obtained from pump–probe measurement, $-\Delta\alpha$ is a result of GSB and SE, ESA leads to $+\Delta\alpha$. The inset depicts the transitions involved in these processes.

Here, $I_w(t, \lambda)$ is the time and wavelength-dependent probe intensity at the detector end when it passes through the optically excited sample, and $I_{w_0}(\lambda)$ is the probe intensity without the pump-induced excitation. The change in probe intensity is given as $\Delta I(t, \lambda) = I_w(t, \lambda) - I_{w_0}(\lambda)$. Output data can also be converted into the change in probe transmittance given as $\Delta T/T$, where T is the probe transmittance without optical excitation. It is related to differential absorption as

$$\Delta\alpha(t, \lambda) = -\log\left(1 + \frac{\Delta T(t, \lambda)}{T(\lambda)}\right) \quad (3)$$

$\Delta\alpha$ can be both negative ($\alpha_w < \alpha_{w_0}$) and positive ($\alpha_w > \alpha_{w_0}$), depending on the processes, as shown in the typical differential absorption spectra of Figure 2b, where dotted line is the resultant $\Delta\alpha$ response. The corresponding change in the sign will also reflect in $\Delta\alpha$ kinetics. A negative $\Delta\alpha$ is a result of ground-state bleaching (GSB) originating from the removal of carriers from the ground state (valence band) due to pump-induced carrier excitation. Therefore, probe absorption (α_w) in an optically excited sample becomes less than that in the nonexcited sample (α_{w_0}). Pump-induced excited carriers can further absorb the probe-beam photons depending on the availability of the states and allowed transitions. These transitions are termed as ESA. Consequently, probe absorption of the excited sample becomes larger than that of the nonexcited sample, leading to a positive $\Delta\alpha$ peak. Both GSB and ESA spectra are schematically shown in Figure 2b, along with the associated transitions in the inset.

Pump-induced excitation is analogous to the population inversion in the system. So, potentially stimulated emission (SE) can also occur for certain wavelengths at the optically allowed transitions with the absorption spectrum Stokes-shifted from that of the ground-state absorption, as shown by the green spectra at a longer wavelength in Figure 2b. A photon from the probe–pulse generates another photon at the same phase and frequency via recombination of the excited carrier.^[58]

3.1. Detailed Setup of Femtosecond Pump–Probe Spectroscopy

The transient absorption spectroscopy (TAS) setup used in this work is shown in **Figure 3a**, depicting the optical bench assembly of different components. Libra optical bench assembly serves as

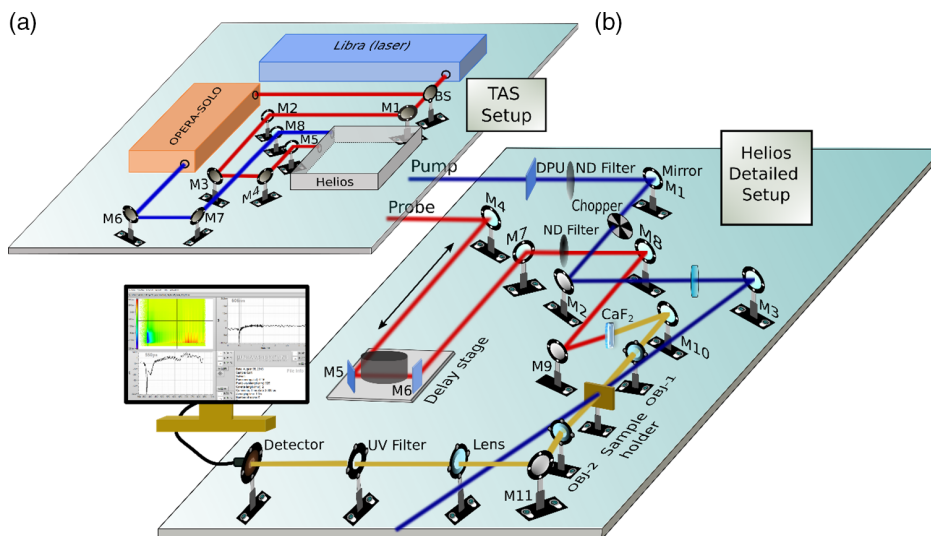


Figure 3. Detailed optical assembly of femtosecond TAS setup. Libra is the laser source, OPERA-SOLO is the optical parametric amplifier, and the HELIOS unit consists of delay optics, sample holder, and detector for measurements.

the laser source for TAS. It comprises four modules; 1) an 800 nm Ti:sapphire mode-locked seed laser with 1 kHz repetition rate, 2) a continuous-wave green diode laser (527 nm) to pump the seed laser, 3) a regenerative amplifier, and 4) a pulse stretcher/compressor. The last two components are required for chirped-pulse amplification (CPA). The Libra uses the CPA technique by stretching a low-energy short-duration pulse initially by $\approx 10\,000$ times using a single-grating pulse stretcher. The regenerative amplifier amplifies the stretched pulse by a factor of ≈ 106 . A single grating compressor then recompresses the pulse nearly to its original duration. Output laser pulse from Libra unit is divided into two paths (pump and probe) by a beam splitter (BS), as shown in Figure 3a. One part of the split beam goes into the OPERA-SOLO unit, output from which serves as the pump-pulse. The other probe-pulse part goes directly into the Helios unit (through mirrors M1–M5). OPERA-SOLO unit is an optical parametric amplifier, providing power amplification along with a mixer unit for pump wavelength tunability. The amplified pump-pulse from OPERA-SOLO enters into the Helios unit through mirrors M6–M8.

The detailed optical bench assembly of the Helios unit is shown in Figure 3b. The probe-pulse passes through a delay line consists of mirrors M4, M5, M6, and M7. It is then directed toward a nonlinear crystal (CaF_2) by the mirrors M8 and M9. The curved mirror M9 focuses the beam on the crystal to generate the white light continuum. The probe-pulse is then aimed toward the sample through the mirror M10 using objective lenses 1 and 2 to adjust the beam path. The excitation pump-beam travels through the center of a neutral density filter (ND filter), depolarizer (DPU), and the optical chopper. A chopper is used to block the alternate pump-pulse to measure the probe signal without pump-induced excitation at each delay time. The alternate pump pulse excites the sample, and the transmitted beam is dumped at the wall. However, the probe-pulse is sequentially moving toward the detector through the focusing objective lens, the mirror M11, a UV filter, another focusing lens, and finally to the detector.

The probe pulse passes through the excited and nonexcited sample alternately, at each time delay. Depending upon the excited carrier dynamics, a part of the probe-beam is absorbed by the sample, and the remaining part is get transmitted. A charge coupled device (CCD) detector at the end receives the transmitted spectra of the probe-beam at each time delay. The amplifier and other elements finally provide a 3D plot of differential absorption as a function of probe wavelength and delay time; an example of such a plot is shown in Figure 5a and discussed later in detail.

4. Fabrication of InGaN/GaN 2D, 1D, and 0D Nanostructures

We have studied and compared the ultrafast nonlinear carrier and photon dynamics in InGaN/GaN nanostructures of various dimensions (varying degree of quantum confinement). InGaN-based QWs (2D), quantum wires (QWIs; 1D)^[65,66] and QDs (0D)^[67,68] are fabricated for this purpose. $\text{In}_{0.14}\text{Ga}_{0.86}\text{N}/\text{GaN}$ QW heterostructure is grown by metalorganic chemical vapor deposition (MOCVD) on a *c*-plane sapphire substrate. A schematic of the complete heterostructure is shown in Figure 4a. The as-grown QW sample is used to fabricate QWI and QD structures via top to bottom dry etching process.

QWI and QD of various dimensions are fabricated using a combination of dry and wet etching processes. Electron beam lithography (EBL) is utilized to transfer the patterns on the planar QW sample. Inductively coupled plasma reactive ion etching (ICP-RIE) is used for dry etching with a combination of Ar (20 sccm), Cl_2 (30 sccm), and BCl_3 (5 sccm) gases, at 60 W radio frequency and 500 W ICP power. Lateral QWIs and vertical-tapered QDs are patterned on the QW sample, as shown schematically in Figure 4b,c, respectively. Post-RIE damages are recovered by the wet etching in boiling phosphoric acid (H_3PO_4) for 5 s, when the dimensions are further reduced. Finally, a treatment in hydrofluoric acid (HF) removes all oxide residues. QWIs of 20 and 50 nm widths and 5 μm length each are fabricated. Fabricated QDs are in the shape

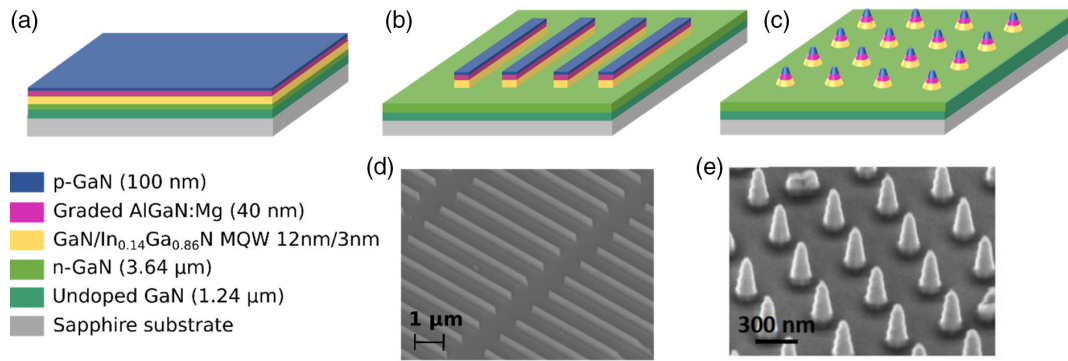


Figure 4. Schematic of a) InGaN/GaN QW heterostructure used in our experiments; b) QWIs, and c) QDs; SEM images of d) fabricated QWIs, and e) QDs.

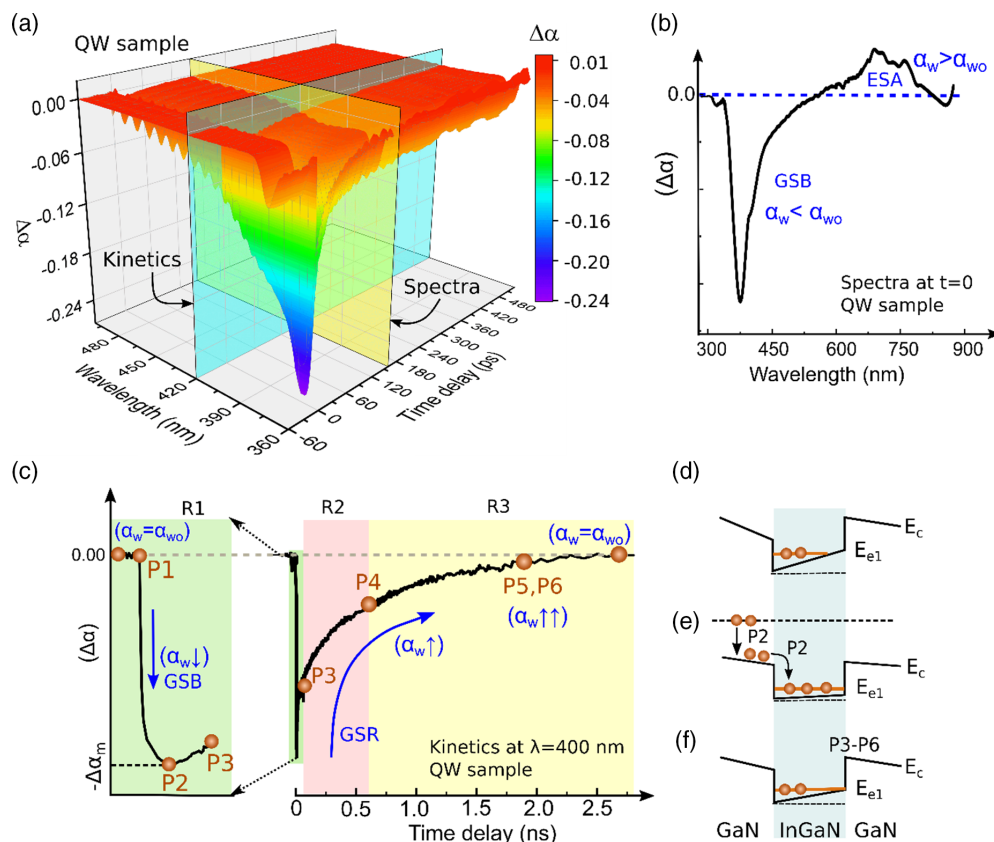


Figure 5. a) 3D plot of differential absorption of QW sample plotted with probe wavelength and time delay, cut along wavelength (time) axis gives the kinetics (spectra) at that wavelength (time); b) differential absorption spectra at zero delay; c) differential absorption kinetics at 400 nm probe wavelength. The initial capture kinetics are shown at the left inset (region R1) and decay kinetics are divided in region R2 and R3; d) CB profile of InGaN/GaN QW at equilibrium, band bending due to polarization is also shown, e) just after optical excitation, bands become flat; f) at a longer time, carrier recombination leads to ground-state recovery.

of disks with a diameter of ≈ 30 nm and height of 3 nm, situated at 22 nm from the base plane of the truncated cone, as shown in the schematics of Figure 4c. Smaller QDs of 12 nm diameter are prepared by the wet treatment of 30 nm QDs with an $\text{H}_3\text{PO}_4/\text{H}_2\text{O}$ (1:5) solution at room temperature for ≈ 1 s. The cross-sectional image of as-fabricated QWIs and QDs taken by scanning electron microscopy (SEM) is shown in Figure 4d,e, respectively.

5. Results and Discussion

Ultrafast TAS (discussed in Section 3.1) with time resolution of ≈ 50 fs is used to measure the carrier dynamics of the fabricated QW, QWI, and QD samples.^[65–67] A 325 nm (< 365 nm) pump-pulse is used to excite the GaN and InGaIn region of the samples. Figure 5a shows the typical 3D plot of differential absorption as a

function of probe wavelength and delay time. Kinetics at each wavelength can be obtained by taking a cut along the wavelength axis. Similarly, spectra at each time delay can be extracted by a cut along the time axis. Figure 5b shows the spectra of the InGaN/GaN QW sample at zero delay ($t = 0$). GSB at the GaN and InGaN band-edges results in a negative $\Delta\alpha$. Figure 5c shows the time-dependent differential absorption kinetics at the InGaN band-edge, where R1, R2, and R3 are three temporal regions. Region R1 is the initial capture kinetics, as shown by the extended scale in the left figure of Figure 5c. Before optical excitation when the system is at equilibrium, probe absorption remains unchanged ($\Delta\alpha = 0, \alpha_w = \alpha_{w0}$). Just after optical excitation, probe absorption (α_w) decreases due to GSB and hot carrier thermalization. Within a few femtoseconds $\Delta\alpha$ reaches a minimum negative value (shown as $-\Delta\alpha_m$) due to the maximum effect of GSB. At this time, most of the carriers are thermalized to the GaN or InGaN band-edges. A single exponential fit of the kinetics in region R1 gives the time constant corresponds to carrier capture into the QW (process P2), which primarily involves electron–electron and electron–phonon scattering (discussed later in detail). Regions R2 and R3 correspond to the decay kinetics (processes P3–P6) when the system equilibrates. Auger recombination and fast carrier trapping into the defect states are dominant in region R2. Slow processes such as radiative recombination and SRH recombination take place in region R3.

5.1. Carrier Capture Kinetics

Thermalization of excess carriers to the band-edge takes place typically on a time scale lesser than 100 fs to few picoseconds.^[65] The detailed process of electron cooling kinetics in a InGaN/GaN QW system is shown in **Figure 6a**, defining each subprocess (A–F) along with the time scale. Holes follow similar cooling mechanisms; however, their thermalization is extremely fast and therefore not a limiting factor. Photoinduced carrier generation at $t = 0$ is instantaneous (process B), and a sharp peak in carrier distribution function $n(E)$ is formed at high energy. Carriers are primarily excited from the GaN region as the

InGaN active region is only 3 nm thick. Therefore, excitation from the InGaN region is not considered in this work. However, carrier capture into the well and carrier thermalization at the GaN band-edge co-occur, shown as processes 1 and 2 in Figure 6b. At 10–100 fs, excited electrons exchange energy via electron–electron scattering until a thermal equilibrium is achieved at a temperature T_c higher than the lattice temperature T_L . Energy renormalization due to carrier–carrier scattering and low-energy phonon emission leads to the Fermi distribution of excited carriers at temperature T_c (process C). From 100 fs to 1 ps, electron–optical phonon scattering (through Fröhlich interaction) sets in due to lattice vibrations, and electrons lose energy by emitting high energy polar optical phonons (POP) (process D). The POP emission mainly dominates carrier capture process due to its high energy (≈ 93 meV for GaN). In the next 1–10 ps, further emission of low-energy phonon modes such as transverse optical phonons (TO) and acoustic phonons takes the system in thermal equilibrium with the lattice temperature T_L (process E).^[56] Once the excited carriers are thermalized to the GaN band-edge and a fraction of these carriers captured into the well, various recombination channels open up for further relaxation (process F, discussed later in detail).

One distinguishing feature in quantum-confined structures is the Pauli state blocking effect. At very high excitation density, localized states (lower energy states occur due to indium inhomogeneity) are saturated by the thermalized carriers. This effect prevents further cooling of the excited carriers to these fully occupied localized states, resulting in Pauli state blocking.^[69] Once recombination processes deplete carriers from the localized energy states, remaining hot carriers fill these states. Therefore, carrier thermalization and relaxation rate can be influenced by the state blocking effect.^[70,71] Figure 6b shows the carrier capture and possible decay transitions of the optically excited InGaN/GaN QW system. Capture time constants at the barrier (GaN) and the well (InGaN) band-edge are shown as τ_c^{GaN} and τ_c^{InGaN} , respectively.

Single exponential fit to the initial $\Delta\alpha$ kinetics gives the capture time constant for a given probe wavelength. Capture time constants at the InGaN band-edge are obtained for QW, QWI, and QD samples. **Figure 7a** shows the obtained capture time

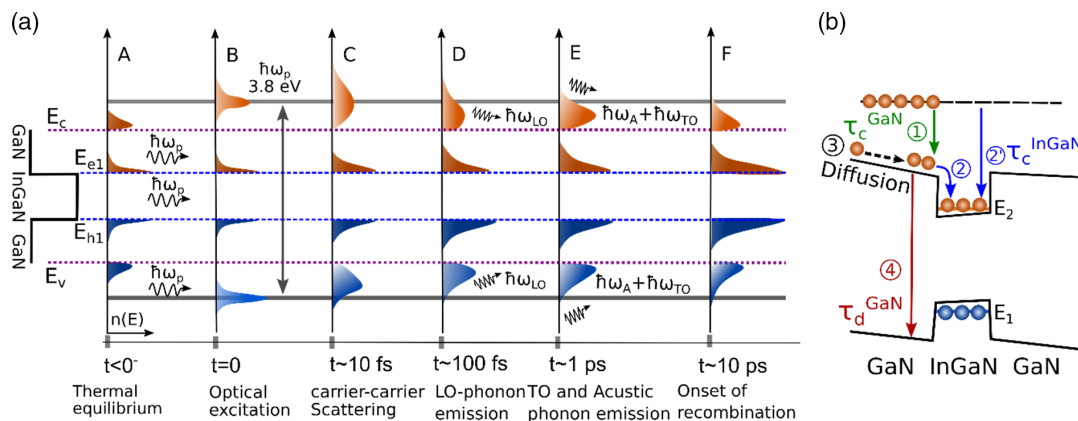


Figure 6. a) The processes involved in carrier thermalization at the GaN band-edge and carrier capture into the InGaN region. Process (A) is the thermal equilibrium, process (B) is optical excitation by 3.8 eV pump-pulse, process (C) is carrier-carrier scattering which leads to energy renormalization and Fermi distribution, process (D) is LO-phonon emission with this carriers from the GaN band-edge captures into the well, process (E) is low energy acoustic phonon emission (of energy $\hbar\omega_A$) for further thermalization, process (F) is the onset of recombination; b) The carrier thermalization at the GaN band-edge (process 1), carrier capture into the well (process 2 and 2'), and carrier decay in the GaN region of an optically excited InGaN/GaN QW system.

constants at the InGaN band-edge (τ_c^{InGaN}) of QW and QWI (having lengths of 20 and 50 nm) samples. Figure 7b–d shows τ_c^{InGaN} of 30 and 20 nm QD samples for varying input pump power, plotted in the vicinity of the InGaN band-edge. Notably, the capture rate slows down with reducing dimensions of both QWIs and QDs, due to a lesser number of states available over a specified energy level for reduced dimensions. Hence, it is imperative that the lower-dimensional QWI (20 nm) and QD (12 nm) samples exhibit a large capture time constant. We have theoretically verified that the capture time constant is varying inversely with the QD radius, by calculating the electron–phonon scattering rate (discussed in detail in Section 5.1), as shown in Figure 7e. The experimentally measured capture time constant of QDs is in good corroboration with the theoretical values. The table in the inset gives the obtained experimental and theoretical values of capture time constant in the active region.^[67]

As shown in Figure 6b, electron capture at the InGaN band-edge involves two steps: 1) carrier thermalization at the GaN band-edge (process 1) and 2) subsequent capture into the InGaN region (process 2). Process 1 is dominated by optical phonon emission, as fewer carriers left at the GaN band-edge right after optical excitation. The fluence-dependent measurement of 20 nm QWIs in Figure 7a and QD samples in Figure 7b–d show a decrease in capture time constant with increasing pump fluence. This indicates that the electron–electron scattering predominantly limits the capture in the InGaN region, as τ_c^{InGaN} is decreasing with increasing pump power (proportional to

excited carrier density). Both the scattering processes (1 and 2) are weakly dependent on energy above the threshold, rendering τ_c^{InGaN} nearly unchanged with the probe wavelength. Apart from the two-step capture process, a small fraction of carriers can directly thermalize to the InGaN band-edge, shown as process 2, in Figure 6b. However, such a process is insignificant due to 3 nm well width and therefore not considered in this work.

5.2. Carrier Diffusion

For a better insight into the carrier dynamics, we have also determined capture time constant at the GaN band-edge (τ_c^{GaN}) for QW and QWI samples, obtained values are shown in Figure 7f. Due to decrease in density of available states near the barrier band-edge (same as InGaN band-edge), capture rate becomes less efficient with increasing confinement in the QWI samples. Carrier capture into the active region essentially depletes carriers from the GaN band-edge. Hence, it is imperative that the τ_c^{InGaN} values should match with the decay time constants at the GaN band-edge. However, the obtained decay time constants at the GaN band-edge are observed to be higher than the respective capture rates at the InGaN band-edge in all the samples. Figure 7g shows the fitted values of the fast decay time constant in the vicinity of the GaN band-edge in QW and QWI samples.^[66] Table 1 shows both the capture and decay time constants at the InGaN and GaN band-edges, respectively, for all the

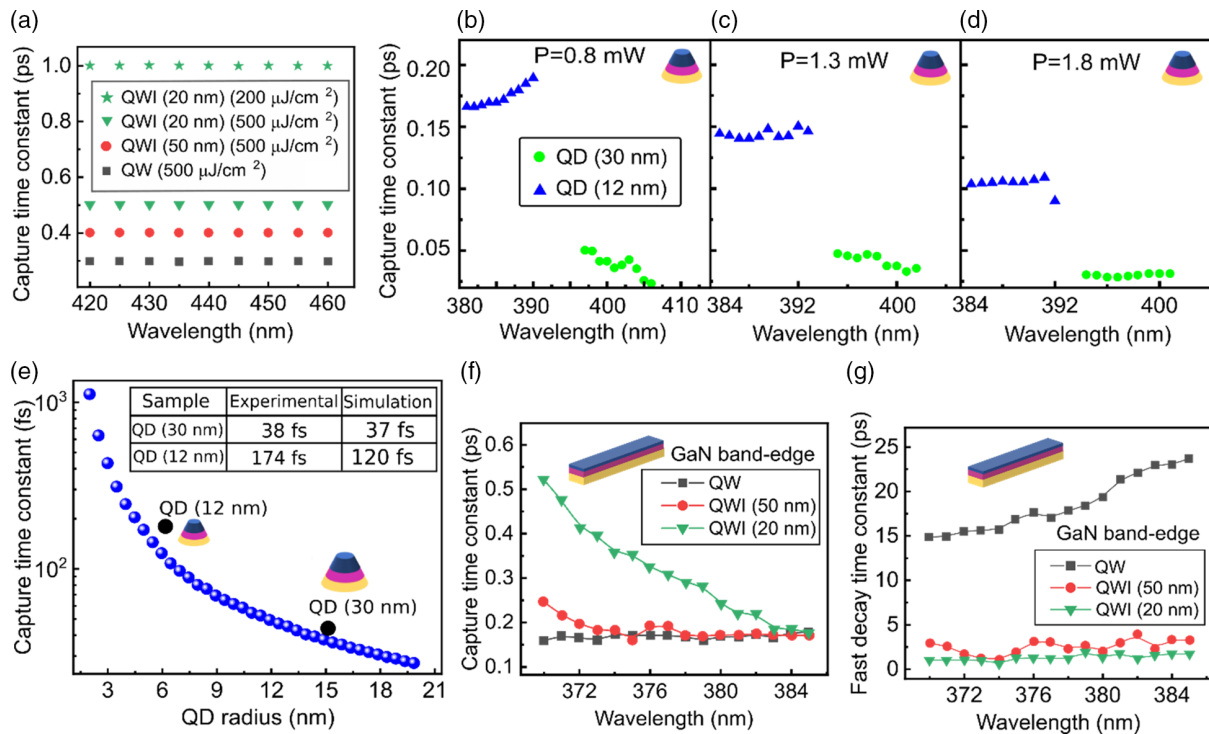


Figure 7. a) Experimentally obtained capture time constants in the vicinity of InGaN band-edge of the QW and QWI (50 and 20 nm, respectively) samples, power-dependent measurement of 20 nm QWIs is also shown therein; b–d) power-dependent capture time constants of 30 and 12 nm QDs; e) simulated capture time constant as a function of QD radius, experimental and theoretical values are tabulated in the inset; f) experimentally obtained capture time constants of QW and QWI samples plotted in the vicinity of the GaN band-edge; g) experimentally obtained fast decay time constants of QW and QWI samples at the GaN band-edge.

Table 1. Measured capture and decay time constants for all the samples.

Samples	Capture time (τ_c^{InGaN}) [fs]	Fast decay time (τ_d^{GaN}) [ps]
QWs	300	15
50 nm QWIs	400	2.5
20 nm QWIs	500	1
30 nm QDs	60	10.7
12 nm QDs	170	12.1

samples. For all the samples, the decay time constants in the barrier region are much higher than that of the capture time constants in the InGaN region. This anomaly indicates that only a fraction of the carriers present in the vicinity is getting captured and contributes to the fast capture rate into the InGaN region. However, a small fraction of the carriers in the barrier region directly recombines into the valence band, shown as process 4 in Figure 6b. In addition, there might be some diffusion limiting carrier supply for the InGaN region, shown as process 3 in Figure 6b.

5.3. Carrier Decay Kinetics

The excess carrier decay kinetics in bulk and the quantum-confined heterostructures are associated with the processes P3–P6, described in Section 1. The kinetics are usually

understood using the A, B, and C models of carrier recombination as^[32]

$$\frac{dn}{dt} = -An - Bn^2 - Cn^3 \quad (4)$$

Here, A (in s^{-1}) corresponds to nonradiative defect-assisted recombination processes. It is an umbrella term used to describe several processes and is classified according to the associated defect energy and physical location. It involves trapping an electron and a hole in the same defect state, leading to their recombination, as shown in Figure 1g. The coefficient B (in cm^3s^{-1}) corresponds to the radiative recombination process. Physically, it involves the transition of an electron from the conduction band (CB) to an empty state in the valence band with the emission of a photon. The coefficient C (in cm^6s^{-1}) corresponds to the non-radiative Auger recombination process. An electron–hole pair recombines, and the released energy is transferred to another electron that is excited to a higher energy level, as shown in Figure 1d. All the possible transitions associated with the processes P4–P6 in the active region are shown in Figure 8a for an InGaN/GaN QW system, just after optical excitation. E_{st} and E_{rc} in the figure represent the shallow trap energy level and nonradiative recombination center, respectively. The coupled differential rate equations describing the system in Figure 8a are given as^[72]

$$\frac{dN_b}{dt} = \frac{I(t)}{qV} - \frac{N_b}{\tau_{\text{cap}}(N_w)} \quad (5)$$

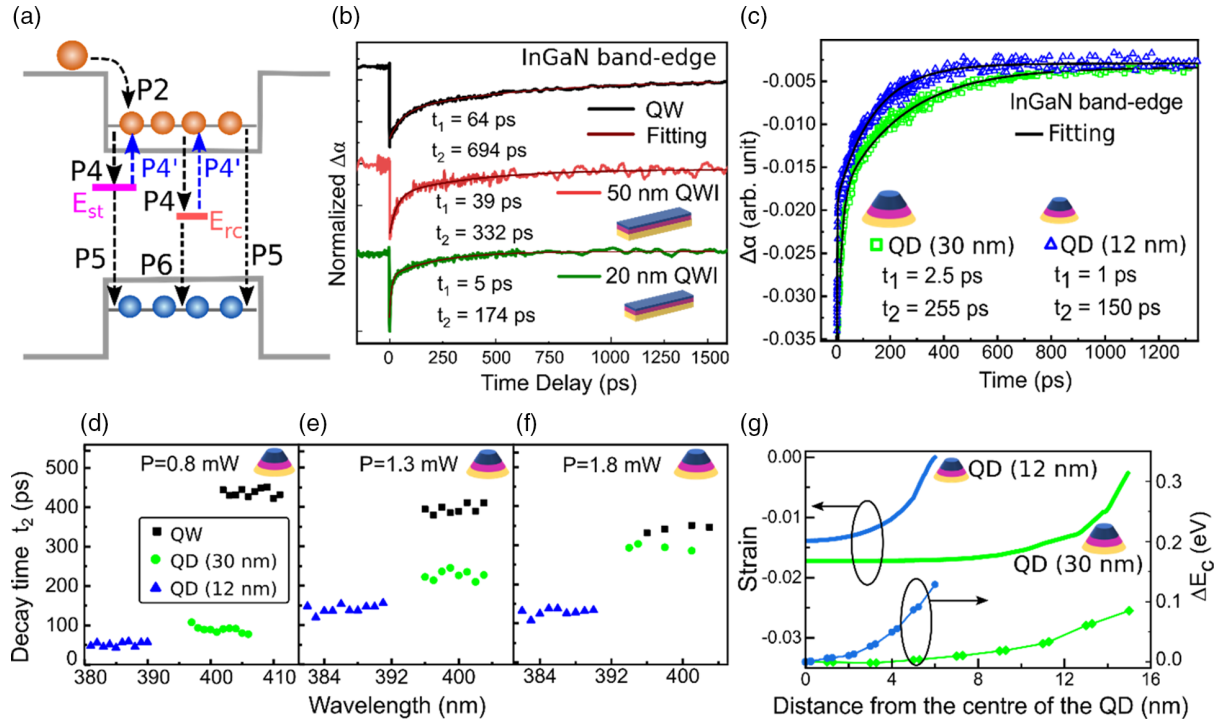


Figure 8. a) Possible transitions during carrier relaxation in the InGaN/GaN QW system; b) experimentally obtained decay kinetics at the InGaN band-edge in QW and QWI (20 and 50 nm, respectively) samples; c) decay kinetics of QD (30 and 12 nm) samples, fitted values are also given therein; d–f) fast decay time constants of QD samples are plotted in the vicinity of the InGaN band-edge with increasing pump power P ; g) theoretically obtained strain and CB offset ΔE_c values along the radial direction. QDs are highly strain-relaxed and bands are flattened at the periphery, creating a natural potential well in the radial direction.

$$\frac{dN_w}{dt} = \frac{N_b}{\tau_{\text{cap}}(N_w)} - \frac{N_w}{\tau_r(N_w)} - N_w \left(\frac{1}{\tau_{\text{et}}^{\text{st}}} - \frac{1}{\tau_{\text{et}}^{\text{rc}}(N_w, N_t)} \right) + P_{\text{st}}N_{\text{st}} + P_{\text{rc}}N_{\text{rc}} \quad (6)$$

$$\frac{dN_{\text{st}}}{dt} = \frac{N_w}{\tau_{\text{et}}^{\text{st}}} - \frac{N_{\text{st}}}{\tau_r(N_{\text{st}})} - P_{\text{st}}N_{\text{st}} \quad (7)$$

$$\frac{dN_{\text{rc}}}{dt} = \frac{N_w}{\tau_{\text{et}}^{\text{rc}}(N_w, N_t)} - \frac{N_{\text{rc}}}{\tau_{\text{ht}}^{\text{rc}}(N_{\text{rc}}, N_t)} - P_{\text{rc}}N_{\text{rc}} \quad (8)$$

Here, N_b and N_w are the carrier densities in the barrier (GaN) and the well (InGaN) region, respectively. N_{st} and N_{rc} are the carrier densities in the shallow and the deep sub-bandgap energy states, respectively, and N_t is the defect density. Time constants associated with capture (process P2) and radiative recombination processes (process P5) are given as τ_{cap} and τ_r , respectively. τ_{et} and τ_{ht} are the electron- and hole-trapping time constants (process P4) associated with SRH recombination (P6). The probability terms P_{rc} and P_{st} in Equation (6)–(8) are discussed later in Section 5.4.

As TAS measures the absorption kinetics, it captures both radiative as well as nonradiative recombination processes. The $\Delta\alpha$ kinetics at the InGaN band-edge is shown in Figure 8b for QW and QWI (20 and 50 nm) samples, and in Figure 8c, for 30 and 12 nm QD samples. Once the carriers are captured into the active region, recombination occurs through the aforementioned processes, and $\Delta\alpha$ tends to increase. A biexponential fit to the temporal regions R2 and R3 gives the fast (t_1) and the slow (t_2) decay time constants, respectively. Both the decay time constants exhibit strong size dependence, as evident from the obtained time constant values shown in Figure 8b,c. Faster time constant t_1 is ascribed to the Auger recombination (process P3) and electron trapping into the sub-bandgap defect states (process P4), which serve as nonradiative SRH recombination centers at a longer time. It is evident from t_1 values that the processes progressively become faster with increasing confinement. As t_1 decreases from 64 ps for QW sample to 5 ps for 20 nm QWI sample. It further decreases from 2.5 ps for 30 nm QDs to 1 ps for 12 nm QDs, as shown in Figure 8c. This observation is attributed to the increased surface defects with increasing quantum confinement, having originated from a larger surface-to-volume ratio and dry etching process. A surge in the availability of surface-induced sub-bandgap states tends to increase the electron-trapping rate in the defect states. An increase in surface-to-volume ratio also escalates the nonradiative surface-recombination rate. However, surface passivation of these nanostructures can help to suppress the surface-induced defects.

The slower time constant t_2 is associated with the radiative recombination processes (process P5). It becomes faster with increasing confinement as t_2 decreases from 694 ps for QW to 332 (174) ps for 50 (20) nm QWI. A significant decrease in t_2 from 255 to 150 ps is also observed in 30 and 12 nm QD samples, respectively. An enhanced exciton binding energy and improved electron-hole wavefunction overlap in quantum-confined structures lead to an increase in the radiative recombination rate, which is desirable to improve the internal quantum efficiency of the active region to realize efficient light emitters. In contrast with the slight reduction in t_1 values, a drop in t_2 values is

substantial with increasing confinement. Therefore, the fast radiative process overcomes the increase in electron-trapping rate, and overall improvement in the luminescence efficacy of QWI and QD is observed. This effect is evident from the internal quantum efficiency (IQE) of these samples obtained from the ratio of room temperature to 10 K photoluminescence (PL) intensity. IQE for QW, 50 nm, and 20 nm QWIs are obtained as 41%, 49%, and 57%, respectively.^[65] IQE of 30 nm QD sample is obtained to be 70%, and 12 nm QD sample is 78%.^[68]

For better insight, slow time constant t_2 is plotted in the vicinity of InGaN band-edge for QD and QW samples with increasing pump power, as shown in Figure 8d–f, respectively. It is evident that t_2 is almost unchanged near the InGaN band-edge. With increasing pump power, t_2 is observed to be reducing in the QW sample. This is attributed to the fact that generated carrier density is higher at higher pump-power, which results in an increased Auger recombination rate, hence enhancing the effective decay rate of the carriers in the QW. On the contrary, the t_2 time constant in QD samples increases at higher pump powers. These QDs are proved to be strain-relaxed near the periphery, resulting in high bandgap near the edges. As shown in Figure 8g, where theoretically calculated strain distribution and CB offset ΔE_c are plotted along the c axis (from center to periphery). The degree of strain relaxation is higher for smaller (12 nm) QDs. A high bandgap near the edges creates a potential well at the center and eventually reduces the effective radius of the QD from that of its physical dimension. However, upon optical excitation, increased carrier density flattens the bands, and increased width of as-formed potential well leads to a larger effective radius of the QD. Excitation carrier density increases with input pump power, thereby increasing the effective dimension of the QD which further translates into reduced oscillator strength. This effect leads to an increase in radiative time constant t_2 .^[67] Reduced injection current density due to the increased effective area for higher carrier injection can mitigate the efficiency droop in these QDs. Therefore, quantum confinement can improve device performance when used as an active region.

5.4. Carrier Recovery from Sub-Bandgap States

Sub-bandgap states, shown in Figure 8a, are categorized mainly as 1) shallow trap levels (E_{st}), and 2) nonradiative recombination centers (E_{rc}). During InGaN growth, there is always an inevitable inhomogeneity in indium composition, creating shallow trap levels below the nominal ground-state energy.^[41,72,73] In addition, defect density also forms deep recombination centers within the bandgap. We have demonstrated that the trapped electrons in these sub-bandgap states do not necessarily make a transition to the valence band and recombine (radiatively or nonradiatively) with holes. Instead, they can emit back to the CB due to screened Coulombic interaction with the electrons in the CB. We have established the probability of carrier escape from these sub-bandgap states and manifested this through TAS.^[72] This phenomenon is shown in Figure 9a, and marked as a transition process P4' in Figure 8a (as it is the reverse process of electron trapping, process P4).

A two-particle Hamiltonian system under Coulombic interaction is considered for computing the detrapping probability of the

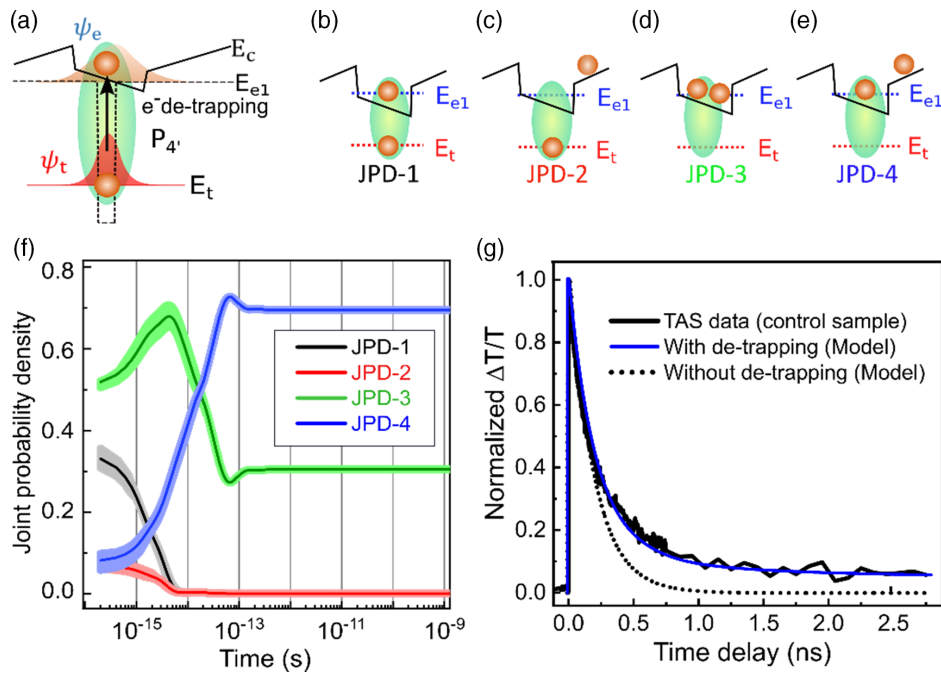


Figure 9. a) Schematic of electron detrapping from sub-bandgap state (E_t) to the nominal ground state E_{e1} of the QW; b–e) four possible outcomes of joint probability density are depicted, b) JPD1: where one electron is in trap state and the other electron is in the QW, c) JPD2: one electron is in the trap state and another is outside the QW, d) JPD3: both electrons are in the QW, e) JPD4: one electron is in the QW and one is outside the QW; f) time evolution of JPDs; g) experimentally obtained excess carrier kinetics ($\Delta\alpha$ kinetics) is plotted with the simulated kinetics. The theoretical model including electron detrapping is giving the best match with the experimental kinetics.

trapped electrons. In such a system, one electron is in the nominal ground state of the QW (E_{e1} , ψ_e) and another electron is trapped in any of the sub-bandgap states (E_t , ψ_t), with ψ_e and ψ_t as the wavefunctions of the respective energy states. The system is schematically shown in Figure 9a. The corresponding wavefunctions along with Coulombic interaction are also shown therein. Screened Coulombic interaction leads to electron–electron scattering and serves as the perturbation to the system. The time-dependent Schrödinger equation is solved numerically for this perturbed two-particle Hamiltonian system. Time evolution of the antisymmetric wavefunction is obtained under simultaneous exchange of spin and coordinates of this Fermionic quasiparticle system.

The time-dependent joint probability density (JPD) of the two-electron interaction is estimated by taking the projection of the Fermionic wavefunction onto the original eigenstate.^[72] There can be four probabilistic outcomes from the interaction, shown as JPD1 to JPD4 in Figure 9b–e. Time evolutions of JPDs are shown in Figure 9f. The probability of finding the electron in the trap potential (JPD1 and JPD2) decreases with time. It reduces to a negligible value in <10 fs and trapped electron is likely to be emitted to the QW. There is a finite probability of ≈ 0.3 (JPD3) for both the electrons present in the well. JPD4 (≈ 0.7) is associated with the situation that one electron is in the QW, whereas the other electron is in the barrier. For both JPD3 and JPD4, the electron is escaped into the QW. This detrapping probability (JPD3 and JPD4) is included as a quantum correction (P_{st} , P_{rc}) to the shallow and deep trap levels (E_{st} , E_{rc}) in the rate Equation (6)–(8). Upon solving these rate equations numerically, with and without quantum correction, the rate of

change of excess carrier density in the well (N_w) is compared with the experimental carrier kinetics obtained from TAS. Experimental data are matching perfectly with the simulation model, which includes quantum correction (P_{st} , P_{rc}), shown as a solid blue line in Figure 9g. Hence, electron escape from the sub-bandgap states should be included in carrier decay kinetics for a more accurate description of the system.

5.5. Quantum-Confined Stark Effect

The natural crystal structure of III–V compound semiconductors such as GaN, InN, and AlN is wurtzite, and they exhibit a hexagonal symmetry. Two types of polarization fields dominate these materials: spontaneous polarization (SP) and piezoelectric polarization (PZ). SP arises due to an inherent asymmetry in the wurtzite crystal structure, whereas PZ arises due to strain at a heterointerface. Both SP and PZ manifest as sheet charges on the surface. For a pseudomorphic $\text{In}_x\text{Ga}_{1-x}\text{N}$ layer on the GaN substrate, the SP and PZ fields become antiparallel.^[74] Therefore, in thermal equilibrium, the InGaN/GaN QW heterostructure's band diagram exhibits band bending in the InGaN region, as shown in Figure 5d. SP is present in both the well and the barrier regions, whereas PZ is only present in the strained QW region.

Upon optical excitation, a fraction of the excited carriers is captured into the well, thereby modifying the charge distribution in the well. This excess charge screens the polarization fields, and the bands become flat, as shown in Figure 5e. Moreover, it

changes the electrostatic confinement potential in the InGaN region and results in an increase in ground state energy of the QW. As carriers recombine via processes P3–P6 (after point P3 in Figure 5c), the polarization field dominates, and the ground-state energy decreases back along with the band bending, as shown in Figure 5f. Redshift in the absorption peak with delay time can be observed due to carrier recombination, which reduces the ground-state energy. This phenomenon is termed as time-dependent quantum-confined Stark effect (QCSE), leading to an undesirable spectral broadening and therefore needs to be minimized for lighting applications.

The overall peak position of differential absorption spectra may also be modified by the Stokes shift (blueshift) and bandgap renormalization (redshift) at high excitation density.^[75] While Stokes shift moves the peak position towards a shorter wavelength with respect to the PL peak, the dynamic change in carrier density shifts the absorption peak as a function of time (QCSE). The evolution of the peak absorption wavelength in QW and QWI samples is shown in Figure 10a. It is noteworthy that the QW sample shows the largest redshift (QCSE) of ≈ 15 nm, whereas the peak wavelength of 50 and 20 nm QWIs shows a ≈ 2 nm redshift. This observation indicates that the InGaN band-edge of the QWI sample largely remains flat for the entire measurement window. This effect is primarily due to strain relaxation and the presence of residual carriers in the well. A similar trend of suppressed QCSE is observed in the QD samples, as QDs are highly strain-relaxed near the periphery, and relaxation is higher for smaller (12 nm diameter) QDs (Figure 8g). Hence, reduced QCSE due to strain relaxation in quantum-confined

heterostructures provides spectral purity in emission spectra. Figure 10 shows the differential absorption and emission spectra of all the samples. Room-temperature PL spectra of QWI and QDs are shown in Figure 10b,c, respectively. The blueshift in emission wavelength is the signature of an increase in ground-state energy due to increased confinement in QWI and QD samples.^[65,67] Corresponding differential absorption spectra of 30 and 12 nm QDs at zero delay is shown in Figure 10d,e, respectively. Figure 10f,g shows the differential absorption spectra of 50 and 20 nm QWIs, respectively, at zero delay.

5.6. Determination of Surface Properties in Planar Semiconductors

The surface properties of semiconductors are very crucial in determining optoelectronic device performance. Dangling bonds at the surface result in sub-bandgap energy states in the active region (as discussed earlier), which eventually serve as nonradiative recombination centers and result in yellow luminescence. In GaN-based transistors, this leads to current leakage and deteriorate the device performance. Therefore, it is of utmost importance that the surface properties be determined and decoupled from their bulk counterpart.

We have used TAS to study the surface properties of two distinct surfaces of planar GaN.^[76,77] Two GaN samples are annealed at high temperatures in oxygen and in nitrogen ambient for comparison of their surface properties. Information of the surface potential obtained from TAS measurements is in

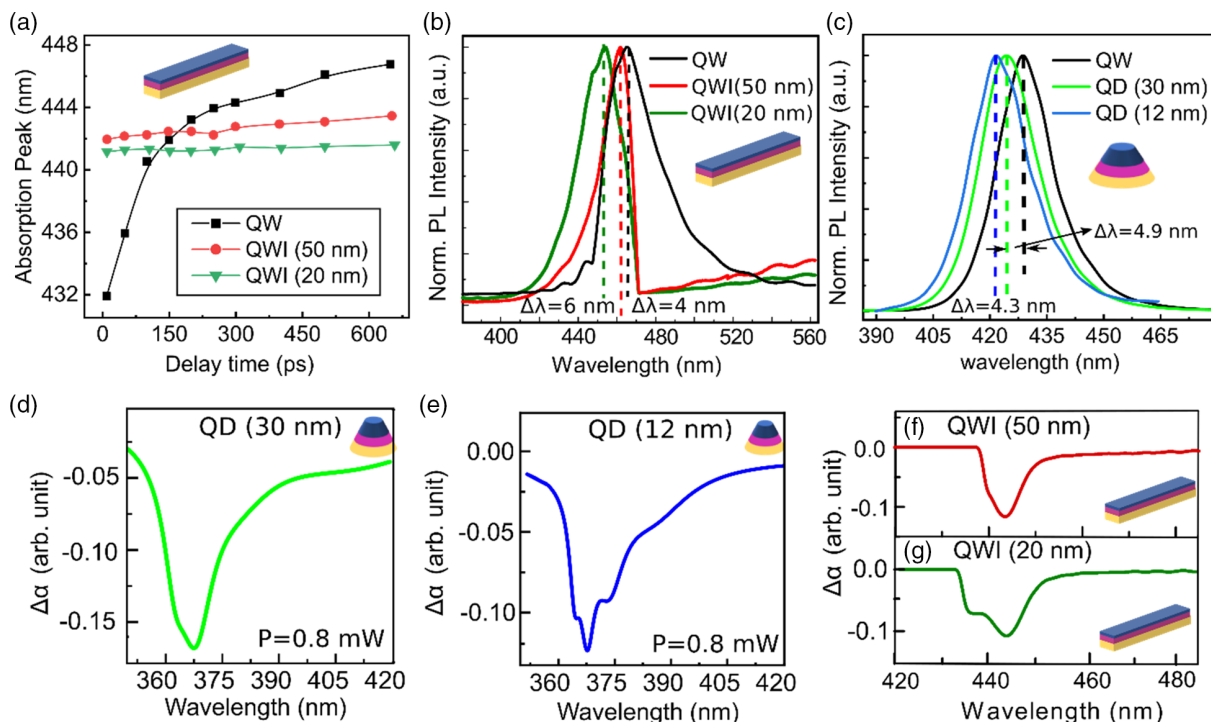


Figure 10. a) Evolution of the absorption peak wavelength at the InGaN band-edge of QW and QWI (50 and 20 nm) samples, QCSE has reduced significantly in QWIs; b) room temperature PL spectra of QWI samples; c) room temperature PL of QD samples. Blueshift in emission wavelength is the signature of increased ground-state energy due to increased confinement; d–g) differential absorption spectra at zero delay of d) 30 nm QD sample, e) 12 nm QD sample; f) 50 nm QWI sample, and g) 20 nm QWI sample.

corroboration with the results measured by Kelvin probe force microscopy (KPFM) technique.^[77] The surface potential of the O₂-treated sample obtained from KPFM is comes out to be 0.65 eV with positive polarity. However, it is 0.45 eV with negative polarity for the N₂-treated sample. Therefore, it is clear that the O₂-rich sample accumulates holes, and the N₂-rich sample accumulates electrons at the surface. The resultant band bending of O₂- and N₂- treated samples are shown in **Figure 11a,b**, respectively. The evolution of surface potential just after optical excitation from $t = 100$ fs to 3 ns is also shown therein. When the samples are subjected to TAS measurement, pump-induced carriers screen the effect of surface potential, and the band becomes flat at the surface at $t \approx 100$ fs. However, as time progresses, the excited carriers recombine through various processes (P3–P6), hence, reducing the screening effect. The surface potential therefore dominates at longer times ($t \approx 3$ ns) which appears as a redshift in the absorption peak of $\Delta\alpha$ spectra, as shown in **Figure 11c,d**, respectively for O₂- and N₂-treated samples. It can be observed that the N₂-rich sample experiences a lesser redshift due to less surface potential (−0.45 eV) as compared with O₂-rich sample (0.65 eV), evident from KPFM measurements. Therefore, information obtained from KPFM is in agreement with that of the TAS data analysis. Thus, by tracing the redshift as a function of delay time, the evolution of surface potential can be established. Time constants associated with the capture process are also extracted near the GaN band-edge (360–380 nm), and obtained values are shown in **Figure 11e**.

It manifests that the N₂-rich sample exhibits a slow capture rate (≈ 200 fs) compared with O₂-rich sample (≈ 160 fs). Carrier capture rate is a measure of the availability of nominal energy states (including shallow sub-bandgap states) over which excited carriers thermalize. A faster capture process signifies the availability of larger surface states in O₂-rich sample.

5.6.1. Decoupling Surface and Bulk Optical Properties

Having understood that the TAS response is intertwined with the surface properties of the samples, it is imperative to decouple the surface and the bulk component from TAS output signal. To establish the relation, we have considered a planar n-type GaN sample of total thickness d , comprising the bulk and surface regions of thicknesses d_b and d_s . The schematic of the structure is shown in the inset of **Figure 12**. The absorbance in bulk and the surface regions are given as α_b and α_s , respectively. The intensity I of the transmitted probe pulse is given as

$$I = I_0 e^{-\alpha_s} e^{-\alpha_b} \quad (9)$$

here, I_0 is the incident intensity of the probe pulse. The measured output signal $\Delta\alpha$ can be expressed as

$$\Delta\alpha(t, \lambda) = (\alpha_{w,s} - \alpha_{wo,s}) + (\alpha_{w,b} - \alpha_{wo,b}) = \Delta\alpha_s + \Delta\alpha_b \quad (10)$$

The decoupling technique of surface and bulk components presented here relies on the fact that d_s remains constant

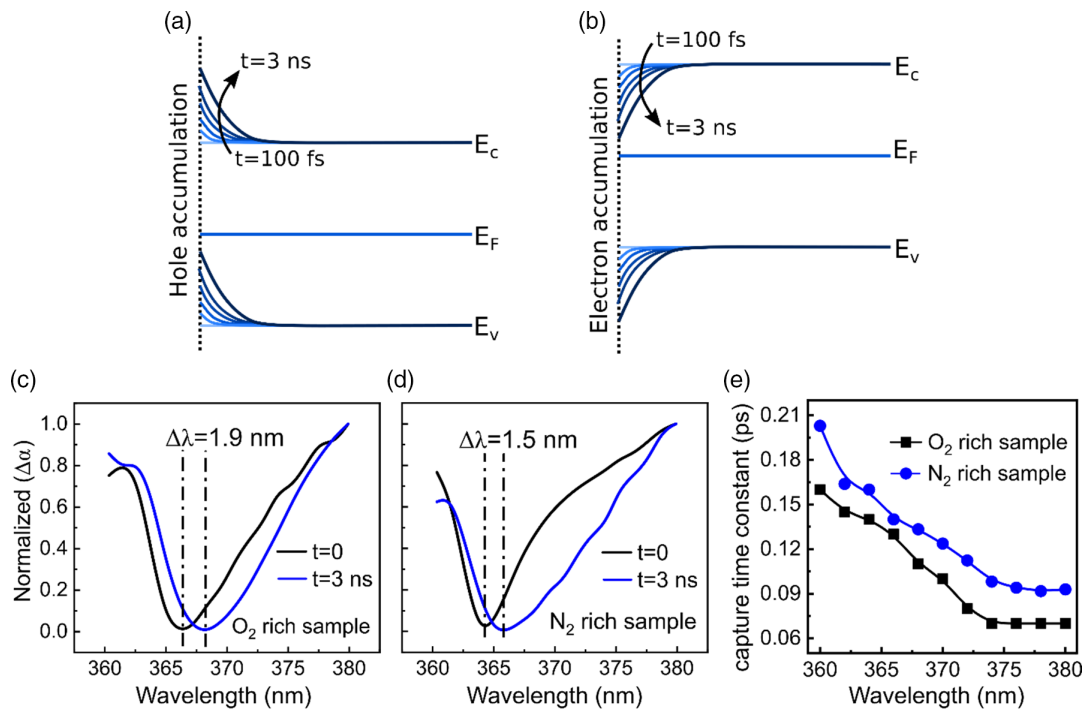


Figure 11. a) Energy band diagram of planar GaN sample is depicted with band-bending at the surface due to surface potential of O₂-treated sample and b) N₂-treated sample. Evolution of surface potential upon optical excitation at $t = 0$ is also depicted from $t = 100$ fs to 3 ns; c) redshift in peak absorption wavelength due to surface potential is shown for O₂ treated sample and d) N₂-treated sample. O₂-treated samples experience a large shift due to higher surface potential; e) experimentally obtained capture time constant of O₂- and N₂-treated samples, O₂-treated sample has faster capture rate due to a large number of surface defect states.

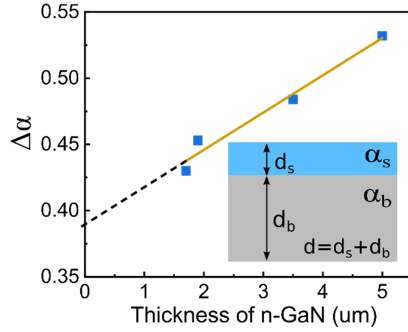


Figure 12. Measured peak differential absorption of bulk n-GaN with varying thickness. Inset depicts the bulk and surface components.

irrespective of the total thickness d . Therefore, the surface absorption remains constant, whereas the bulk absorption varies with d . We thus measured differential absorption for planar structures with various d , i.e., $\Delta\alpha = \Delta\alpha_s + \Delta\alpha_b^n$. Here, superscript n corresponds to the sample with thickness d_n .

The measured differential absorption for the samples with various thicknesses is shown in Figure 12. It is observed that the differential absorption reduces upon reducing the sample thickness due to the reduced absorption. Therefore, limiting case of the sample thickness shrinking to zero gives the differential absorption solely from the surface, i.e.

$$\lim_{d \rightarrow 0} \Delta\alpha = \Delta\alpha_s \quad (11)$$

This value is achieved by extrapolating the measured differential absorption, as shown in Figure 12. After extracting the differential absorption of the surface for all probe delay times, differential absorption in bulk is estimated from Equation (10).

6. Theoretical Calculation of Time Constants

The capture and recombination time constants used in solving the coupled differential rate equations are calculated numerically as a function of carrier density in the well (N_w). In quantum-confined structures, time constants are highly sensitive to the electron–hole wavefunction overlap. Therefore, all transition rates are calculated quantum mechanically using Fermi’s golden rule.

6.1. Electron–Phonon Scattering Rate

Carrier–phonon interaction is one of the most elementary scattering processes that give essential information about several aspects of semiconductor physics, including the study of high field carrier transport, excess carrier thermalization to the band-edge, and carrier capture into the well. In particular, Carrier–phonon scattering in polar semiconductors is dominated by the longitudinal polar optical phonons (POPs), due to their high energy. We have theoretically obtained the carrier capture rate at the InGaN band-edge by calculating the electron–phonon scattering in InGaN/GaN QW and QD. Obtained capture rates are in good agreement with the experimental values measured from TAS.

6.1.1. Capture Rate in QWs

POP scattering rate is calculated for carrier capture from barrier (GaN) to the first bound state in the QW (as it is the most populated energy state in the well). The probability that a carrier in the initial state $|k_i\rangle$ is captured into the QW ground state $|k_f\rangle$ (final state), by emitting LO phonons of wave vector \mathbf{q} , is given by the Fermi’s golden rule^[78]

$$W(k_i, k_f) = \frac{2\pi}{\hbar} (N_q + 1) \sum_{\mathbf{q}} |C|^2 |M|^2 \delta(E(k_f) - E(k_i) + \hbar\omega_{LO}) \quad (12)$$

Here, $E(k_i)$ and $E(k_f)$ correspond to the energy of the initial and the final states, respectively. Longitudinal polar optical phonon energy is given as $\hbar\omega_{LO}$, and the phonon wave number N_q and constant C are given as

$$N_q = \frac{1}{\exp\left(\frac{\hbar\omega_{LO}}{k_B T}\right) - 1}, \quad C = i \left[\frac{2\pi}{V\epsilon_0} e^2 \hbar\omega_{LO} \left(\frac{1}{\epsilon_\infty} - \frac{1}{\epsilon_s} \right) \right]^{1/2} \quad (13)$$

where V is the volume of the active region, $\epsilon_\infty(\epsilon_s)$ is the high-frequency (static) dielectric constant, ϵ_0 is the free space permittivity, e is the electronic charge, k_B is the Boltzmann constant, and T is the temperature. The matrix element M is defined as

$$M = -\frac{C}{q} F(q_z, z) \delta_{k_f - k_i - q} \quad (14)$$

where function $F(q_z, z)$ is given as

$$F(q_z, z) = \int_{-\infty}^{\infty} \psi_f \psi_i^* e^{-iq_z z} dz \quad (15)$$

Here, wavefunction ψ_i corresponds to the continuum states in the barrier region, hence considered as a plane wave, ψ_f is the wavefunction of the first bound state of the QW. Here, q_z is the phonon wave vector in the growth direction (z axis). The total scattering rate for longitudinal polar optical phonon emission per unit volume is given as

$$1/\tau_c^{2D}(k) = \frac{|C|^2}{4\pi^2 \hbar} (N_q + 1) \int d\phi \int dq I_{2D}(q, z) q \delta[E(k - q) - E(k) + \hbar\omega_{LO}] \quad (16)$$

with ϕ being the angle between photon and phonon wavevectors \mathbf{k} and \mathbf{q} , respectively, which satisfies the following relation, $q_\pm = k \cos \phi \pm \sqrt{k^2 \cos^2 \phi - \frac{2m_e^* \omega_{LO}}{\hbar}}$; m_e^* is the effective mass of an electron. Finally, the overlap integral $I_{2D}(\mathbf{q}, z)$ is given as

$$I_{2D}(\mathbf{q}, z) = \int_{-\infty}^{\infty} dq_z \frac{|F(q_z, z)|^2}{q^2 + q_z^2} \quad (17)$$

Equation (16) is solved numerically to obtain the 2D capture time constant τ_c^{2D} of the electrons at the InGaN band-edge. In **Figure 13a**, scattering rate is plotted with E_k (excess energy of electrons in the barrier region). For the electron at the GaN band-edge, excess energy E_k will corresponds to the CB offset

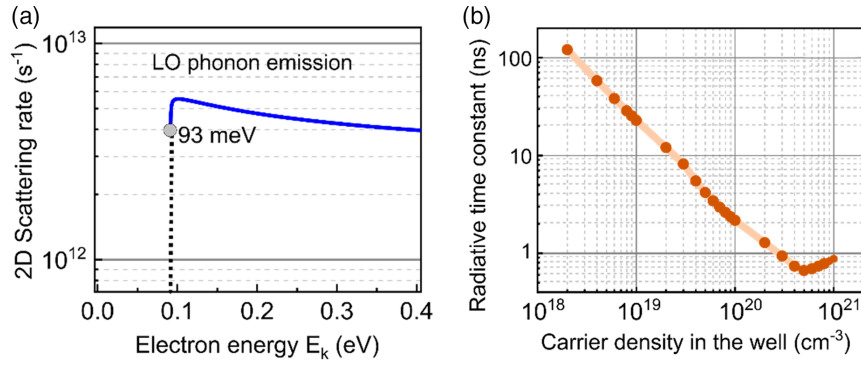


Figure 13. a) Simulated scattering rate for LO polar optical phonon emission in InGaN/GaN QW system. Capture time constant is ≈ 200 fs; b) simulated radiative time constant as a function of carrier density in the well, radiative rate increases with increasing carrier density, slight increase at high carrier density due to optical gain saturation.

at the GaN/InGaN interface ($\Delta E_c \cong 0.26$ eV). LO polar optical phonon emission requires a minimum energy of 93 meV. The scattering rate is in the range of 10^{13} per second (≈ 100 fs), which is in corroboration with the capture time constants obtained from TAS. The scattering rate is observed to decrease at higher energies, as it requires more optical phonons for carriers to thermalize to the band-edge.

6.1.2. Capture Rate in QDs

The capture time constant in QDs shown in Figure 7e is calculated using electron–phonon scattering, by assuming a cylindrical potential well. InGaN/GaN cylindrical potential well of radius R_0 (along radial axis r) and height H (along z axis) is considered to establish the theoretical formalism. As defined earlier in Equation (12), W gives the probability of carrier capture from the initial state $|k_i\rangle$ to the final bound state $|k_f\rangle$. In case of QDs $|k_f\rangle$ is the final bound state in the cylindrical potential well. The capture rate per unit volume in 0D, by summing over initial states with occupation probability $f(E_{k_i})$, is given as^[79,80]

$$\frac{1}{\tau_{c0}^{0D}} = \frac{2\pi}{\hbar} (N_q + 1) \frac{\hbar\omega_{LO}e^2}{2\epsilon_0V} \left(\frac{1}{\epsilon_\infty} - \frac{1}{\epsilon} \right) \sum_k \delta(E(k_f) - E(k_i)) + \hbar\omega_{LO} f(E_{k_i}) \sum_q \frac{|\langle k_f | e^{-iq \cdot r} | k_i \rangle|^2}{q^2} \quad (18)$$

The matrix element term (last term) is obtained by considering cylindrical wavefunctions. The total energy and the corresponding wavefunction of an electron in the first bound state of the cylindrical potential well of radius R_0 and height H is given by^[81]

$$E_{nlm} = \frac{\hbar^2}{2m^*} \left[\left(\frac{q_{lm}}{R_0} \right)^2 + \left(\frac{n\pi}{H} \right)^2 \right] \quad (19)$$

$$\psi_{nlm}(r, \theta, z) = R(r)Z(z)\Theta(\theta) = N_{nlm} J_m \left(\frac{q_{lm}}{R_0} r \right) \sin \left(\frac{n\pi}{H} z \right) e^{im\theta} \quad (20)$$

Here, the quantum numbers l , m , and n are the positive integers with $l, n = 1, 2, 3 \dots$ and $m = 0, 1, 2 \dots$; N_{nlm} is the normalization

factor, J_m is the m th order Bessel function. We have considered the first bound state E_{110} with the corresponding wavefunction $\psi_{110}(r, \theta, z)$ for the POP scattering rate. The calculated capture time constant for InGaN/GaN QDs is in good agreement with the experimental values, as shown in the inset of Figure 7e of Section 5.1.

6.2. Radiative Recombination Rate

Spontaneous radiative recombination rate (R_{sp}) is defined as

$$R_{sp}(\hbar\omega) = \frac{8\pi n_r^2 (\hbar\omega)^2}{h^3 c^2} g_{2D}(\hbar\omega) \left[1 - \exp \left(\frac{\hbar\omega - E_{Fn} + E_{Fp}}{k_B T} \right) \right]^{-1} \quad (21)$$

Here, $\hbar\omega$ is the energy of the emitted photon, c is the velocity of light, E_{Fn} and E_{Fp} are the quasi-Fermi levels for electrons and holes, respectively. Optical gain (g_{2D}) for the QW is obtained from Fermi's Golden Rule^[82]

$$g_{2D}(\hbar\omega) = \frac{1}{n_{well}} \left(\frac{\pi e^2}{n_r c \epsilon_0 (m_e^*)^2 \omega} \right) \sum_{n_z, m_z} |J_{n_z m_z}^{eh}|^2 \times \int_0^\infty dE_t \rho_r^{2D} |\hat{e} \cdot P_{cv}|^2 \times (f_c - f_v) \times \frac{\Gamma_L / (2\pi)}{[E_{n_z m_z}^{eh}(0) + E_t - \hbar\omega]^2 + (\Gamma_L / 2)^2} \quad (22)$$

Here n_r is the refractive index of the active region, n_{well} gives the number of QWs; n_z and m_z are the integers for energy quantization along the z direction (growth axis), in the conduction and the valance bands, respectively; ρ_r^{2D} is the reduced DOS. Energy E_t given as $\hbar^2 k_t^2 / 2m_r$, is the energy of free electron with wavevector k_x and k_y ; here $k_x = k_y = k_t$ and m_r is the reduced mass for electron and hole. Transition energy ($E_{n_z m_z}^{eh}$) is given as^[30]

$$E_{n_z m_z}^{eh} = E_g + \frac{\hbar^2}{2m_e^*} \left(\frac{n_z \pi}{L_z} \right)^2 - \frac{\hbar^2}{2m_h^*} \left(\frac{m_z \pi}{L_z} \right)^2 \quad (23)$$

Here, $f_c(f_v)$ is the Fermi–Dirac distribution functions for electrons (holes). Last term in Equation (22) is Lorentzian function for linewidth broadening, caused by various scattering events;

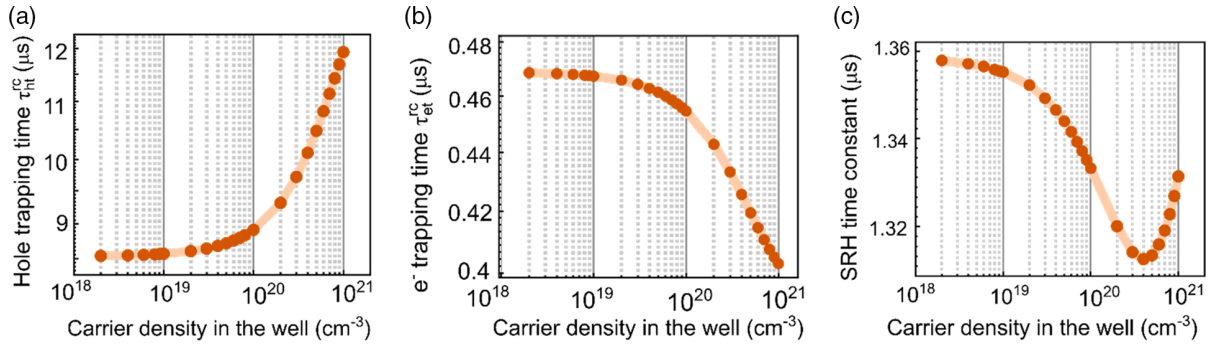


Figure 14. a) Simulated hole-trapping time constant; b) electron-trapping time constant; c) total SRH time constant as a function of carrier density in the QW. Slow hole trapping is the limiting factor for slow SRH recombination rate.

here, Γ_L is the linewidth factor. The optical momentum matrix element is given as

$$|\langle \psi_e | p | \psi_h \rangle| = |\hat{e} \cdot P_{cv} \delta_{k,k_v} | I_{n_z m_z}^{eh} | \quad (24)$$

where ψ_e (ψ_h) is the electron wavefunctions and p is the momentum operator. Overlap integral ($I_{n_z m_z}^{eh}$) and polarization-dependent matrix element term $|\hat{e} \cdot P_{cv}|$ is expressed as

$$I_{n_z m_z}^{eh} = \int_{-\infty}^{\infty} \phi_c^*(z) \phi_v(z) dz \quad \text{and} \quad |\hat{e} \cdot P_{cv}| = |\langle u_c | \hat{e} \cdot P | u_v \rangle| \quad (25)$$

Here, $\phi_c(z)$ and $\phi_v(z)$ are the wavefunctions in the z direction, P is the polarization, \hat{e} is the unit vector in the direction of optical electric field. The overlap integral is obtained by solving for ψ_e and ψ_h from the self-consistent Schrödinger–Poisson equations. We have considered only the first sub-band transitions in our calculations. Figure 13b shows the simulated radiative recombination time constant as a function of carrier density in the well. The radiative recombination rate increases with carrier density. It is in the range of 700–500 ps at high carrier density, which we have also obtained from TAS. However, a slight decrease in radiative time constant is observed at higher carrier density due to optical gain saturation.

6.3. Nonradiative SRH Recombination Rate

In SRH recombination, electron is trapped into a deep recombination center followed by a hole trapping, as shown in Figure 1g. For quantum-confined systems, SRH rate is strongly depend on the electron and hole wavefunction overlap, which changes significantly with applied field due to QCSE. We have considered a field-assisted multiphoton emission process to calculate the electron- and hole-trapping rates for a InGaN/GaN QW system. Midbandgap defects are considered in our calculation. Electron-(hole-)trapping rate C_e (C_h) is given as^[83,84]

$$C_{\left[\begin{smallmatrix} e \\ h \end{smallmatrix} \right]} = \frac{16\pi^2 a^3}{\hbar} (\Delta E - S\hbar\omega_{LO})^2 \left| \psi_{\left[\begin{smallmatrix} c \\ v \end{smallmatrix} \right]}(z) \right|^2 G(\Delta E) \quad (26)$$

Here, $a = \hbar/\sqrt{2m_e^* \Delta E}$ is the Bohr radius of the trapped electron at energy E_{rc} (mid-bandgap), ΔE is the energy difference between the first bound state (E_{e1}) and the defect state (E_{rc}), $\hbar\omega_{LO}$ is the

phonon energy associated with the electron trapping, S is the Huang–Rhys factor; the auxiliary function $G(\Delta E)$ is given as

$$G(\Delta E) = \frac{1}{\hbar\omega_{LO}\sqrt{2\chi}} \left(\frac{\xi}{P_N + \chi} \right)^{P_N} \exp\left(\chi - (2N_q + 1)S + \frac{\Delta E}{2kT} \right) \quad (27)$$

where P_N is given as $\Delta E/\hbar\omega_{LO}$ and it accounts for the average number of phonons involved in the capture process; variables, $\xi = 2S\sqrt{N_q(N_q + 1)}$, and $\chi = \sqrt{P^2 + \xi^2}$. Neglecting the background carrier concentration after optical excitation, SRH recombination rate ($1/\tau_{SRH}$) is obtained by integrating C_e and C_h within the QW width (along the z axis)

$$\frac{1}{\tau_{SRH}} = \int N_t \left(\frac{c_e c_h}{c_e + c_h} \right) dz \quad (28)$$

where N_t is the defect density, electron- and hole-trapping time constants in the deep traps are defined as τ_{et}^{tc} and τ_{ht}^{tc} , respectively, as mentioned in the rate equations (6)–(8). They are obtained individually as, $\tau_{et}^{tc} = 1/\int N_t c_e dz$ and $\tau_{ht}^{tc} = 1/\int N_t c_h dz$, respectively. In Figure 14a,b, simulated electron- and hole-trapping rates are shown respectively, as a function of carrier density in the well. The hole-trapping rate is slower than the electron-trapping rate, hence, holes are limiting the SRH recombination rate at high carrier density, as shown in Figure 14c where SRH time constant is plotted.

7. Conclusion

In conclusion, we have used femtosecond pump–probe absorption spectroscopy to investigate the ultrafast nonlinear carrier and photon dynamics in InGaN/GaN-based quantum-confined nanostructures. We have fabricated QW, QWI, and QD samples and investigate the effect of carrier confinement on the ultrafast dynamics of these samples. The basic principle and detailed setup of TAS is also discussed. Carrier capture and relaxation processes are studied extensively. It is observed that the carrier capture at the InGaN band-edge becomes less efficient in the QWI and QD samples due to reduced DOS. Excess-carrier decay kinetics also exhibit strong size dependency. Fast time constant associated with the carrier trapping in sub-bandgap states has reduced in smaller dimensions due to increased surface-induced

Table 2. Summary of the information obtained from ultrafast TAS analysis.

Samples	QW (2D)	QWI (1D)	QD (0D)
Capture time constant (τ_{c}^{InGaN} and τ_{c}^{GaN})	Low	Moderate	High
(Fast) trapping time constant (t_1)	High	Moderate	Low
(Slow) radiative time constant (t_2)	High	Moderate	Low
QCSE	High	Low	Low
IQE	Low	Moderate	High

defect states, originated from dry etching and large surface-to-volume ration. Enhanced radiative recombination due to increased exciton binding energy, and improved electron–hole wavefunction overlap is the key observation in QWI and QD samples. This results in an improved IQE in smaller dimension nanostructures. Carrier diffusion dynamic in the barrier region is also explored. A novel phenomenon of carrier recovery from sub-bandgap states is demonstrated in the QW sample using TAS decay kinetics. Rate equations are solved numerically, and a quantum correction is introduced to accommodate the carrier detrapping. TAS facilitates the real-time monitoring of time-dependent QCSE at the InGaN band-edge. Suppressed QCSE is observed in QWIs and QDs due to strain relaxation, which results in spectral purity and reduces FWHM in these samples. **Table 2** shows the observations qualitatively.

Experimentally obtained capture and decay time constants are in good agreement with our numerically calculated values of the time constants. Capture and decay time constants are obtained considering electron and hole wavefunction. Polar optical phonon emission through electron–phonon scattering is calculated to obtain the 2D and 0D capture time constants in the InGaN region, which are in the range of ≈ 100 fs. Radiative and SRH recombination rates are also obtained as a function of excess carrier density in the well using Fermi's golden rule. Radiative recombination rate tends to increase (800–600 fs) at high carrier density. SRH time constant is ≈ 1.3 μs , and it is found to be less sensitive to carrier density in the well.

In addition to this, surface properties of O_2 - and N_2 -treated planar GaN samples are also examined using TAS. We have used TAS as a nondestructive technique to investigate the surface potential.

Acknowledgements

This work was partially supported by the Department of Science and Technology.

Conflict of Interest

The authors declare no conflict of interest.

Data Availability Statement

Research data are not shared.

Keywords

carrier dynamics, InGaN/GaN nanostructures, pump–probe spectroscopy, transient absorption spectroscopy

Received: May 25, 2021

Revised: July 11, 2021

Published online: July 29, 2021

- [1] R. N. Hall, G. E. Fenner, J. D. Kingsley, T. J. Soltys, R. O. Carlson, *Phys. Rev. Lett.* **1962**, 9, 366.
- [2] J. I. Pankove, *Phys. Rev. Lett.* **1962**, 9, 283.
- [3] M. I. Nathan, W. P. Dumke, G. Burns, F. H. Dill, G. Lasher, *Appl. Phys. Lett.* **1962**, 1, 62.
- [4] H. P. Maruska, J. J. Tietjen, *Appl. Phys. Lett.* **1969**, 15, 327.
- [5] B. Monemar, *Phys. Rev. B* **1974**, 10, 676.
- [6] R. Dingle, D. D. Sell, S. E. Stokowski, M. Ilegems, *Phys. Rev. B* **1971**, 4, 1211.
- [7] J. I. Pankove, *J. Lumin.* **1973**, 7, 114.
- [8] M. Sano, M. Aoki, *Jpn. J. Appl. Phys.* **1976**, 15, 1943.
- [9] H. P. Maruska, D. A. Stevenson, J. I. Pankove, *Appl. Phys. Lett.* **1973**, 22, 303.
- [10] P. Upadhyay, D. Saha, *Phys. Status Solidi A* **2018**, 215, 1800174.
- [11] S. Yoshida, S. Misawa, S. Gonda, *Appl. Phys. Lett.* **1983**, 42, 427.
- [12] H. Amano, N. Sawaki, I. Akasaki, Y. Toyoda, *Appl. Phys. Lett.* **1986**, 48, 353.
- [13] S. Yamasaki, S. Asami, N. Shibata, M. Koike, K. Manabe, T. Tanaka, H. Amano, I. Akasaki, *Appl. Phys. Lett.* **1995**, 66, 1112.
- [14] S. Nakamura, T. Mukai, *Jpn. J. Appl. Phys.* **1992**, 31, L1457.
- [15] S. Nakamura, M. Senoh, T. Mukai, *Appl. Phys. Lett.* **1993**, 62, 2390.
- [16] S. Nakamura, *J. Vac. Sci. Technol., A* **1995**, 13, 705.
- [17] S. Nakamura, T. Mukai, M. Senoh, *Appl. Phys. Lett.* **1994**, 64, 1687.
- [18] R. Sarkar, K. Ghosh, S. Bhunia, D. Nag, K. R. Khiangte, A. Laha, *Nanotechnology* **2019**, 30, 065603.
- [19] R. P. Prasankumar, P. C. Upadhyay, A. J. Taylor, *Phys. Status Solidi B* **2009**, 246, 1973.
- [20] V. Pendem, P. K. Saha, S. Chouksey, S. Ganguly, D. Saha, *J. Lumin.* **2021**, 229, 117703.
- [21] V. Pendem, A. Udai, T. Aggarwal, S. Ganguly, D. Saha, *Nanotechnology* **2019**, 30, 274002.
- [22] R. A. Arif, H. Zhao, Y. K. Ee, N. Tansu, *IEEE J. Quantum Electron.* **2008**, 44, 573.
- [23] Y.-K. Song, M. Kuball, A. V. Nurmikko, G. E. Bulman, K. Doverspike, S. T. Sheppard, T. W. Weeks, M. Leonard, H. S. Kong, H. Dieringer, J. Edmond, *Appl. Phys. Lett.* **1998**, 72, 1418.
- [24] H. Y. Ryu, K. H. Ha, S. N. Lee, T. Jang, J. K. Son, H. S. Paek, Y. J. Sung, H. K. Kim, K. S. Kim, O. H. Nam, Y. J. Park, J. I. Shim, *IEEE Photon. Technol. Lett.* **2007**, 19, 1717.
- [25] A. Aiello, Y. Wu, A. Pandey, P. Wang, W. Lee, D. Bayerl, N. Sanders, Z. Deng, J. Gim, K. Sun, R. Hovden, E. Kioupakis, Z. Mi, P. Bhattacharya, *Nano Lett.* **2019**, 19, 7852.
- [26] A. Banerjee, F. Dogan, J. Heo, A. Manchon, W. Guo, P. Bhattacharya, *Nano Lett.* **2011**, 11, 5396.
- [27] J. Heo, S. Jahangir, B. Xiao, P. Bhattacharya, *Nano Lett.* **2013**, 13, 2376.
- [28] T. Frost, S. Jahangir, E. Stark, S. Deshpande, A. Hazari, C. Zhao, B. S. Ooi, P. Bhattacharya, *Nano Lett.* **2014**, 14, 4535.
- [29] W. Guo, M. Zhang, A. Banerjee, P. Bhattacharya, *Nano Lett.* **2010**, 10, 3356.
- [30] T. Aggarwal, V. Pendem, A. Udai, P. K. Saha, S. Chouksey, S. Ganguly, D. Saha, *Jpn. J. Appl. Phys.* **2019**, 58, SCCC15.

- [31] M. A. Johar, H.-G. Song, A. Waseem, J.-H. Kang, J.-S. Ha, Y.-H. Cho, S.-W. Ryu, *Nanoscale* **2019**, *11*, 10932.
- [32] J. Piprek, F. Römer, B. Witzigmann, *Appl. Phys. Lett.* **2015**, *106*, 101101.
- [33] P. Bhattacharya, D. Basu, A. Das, D. Saha, *Semicond. Sci. Technol.* **2011**, *26*, 014002.
- [34] D. Banerjee, S. Sankaranarayanan, D. Khachariya, M. B. Nadar, S. Ganguly, D. Saha, *Appl. Phys. Lett.* **2016**, *109*, 031111.
- [35] M. Zhang, P. Bhattacharya, W. Guo, *Appl. Phys. Lett.* **2010**, *97*, 011103.
- [36] S. Jahangir, T. Schimpke, M. Strassburg, K. A. Grossklaus, J. M. Millunchick, P. Bhattacharya, *IEEE J. Quantum Electron.* **2014**, *50*, 530.
- [37] C. Zhao, T. K. Ng, A. Prabaswara, M. Conroy, S. Jahangir, T. Frost, J. O'Connell, J. D. Holmes, P. J. Parbrook, P. Bhattacharya, B. S. Ooi, *Nanoscale* **2015**, *7*, 16658.
- [38] D. Banerjee, K. Takhar, S. Sankaranarayanan, P. Upadhyay, R. Ruia, S. Chouksey, D. Khachariya, S. Ganguly, D. Saha, *Appl. Phys. Lett.* **2015**, *107*, 101108.
- [39] T. Frost, A. Hazari, A. Aiello, M. Z. Baten, L. Yan, J. Mirecki-Millunchick, P. Bhattacharya, *Jpn. J. Appl. Phys.* **2016**, *55*, 032101.
- [40] M. Zhang, A. Banerjee, C.-S. Lee, J. M. Hinckley, P. Bhattacharya, *Appl. Phys. Lett.* **2011**, *98*, 221104.
- [41] D. Nag, R. Sarkar, S. Bhunia, T. Aggarwal, K. Ghosh, S. Sinha, S. Ganguly, D. Saha, R.-H. Horng, A. Laha, *Nanotechnology* **2020**, *31*, 495705.
- [42] A. Banerjee, T. Frost, S. Jahangir, P. Bhattacharya, *IEEE J. Quantum Electron.* **2014**, *50*, 228.
- [43] D. Nag, T. Aggarwal, S. Sinha, R. Sarkar, S. Bhunia, Y.-F. Chen, S. Ganguly, D. Saha, R.-H. Horng, A. Laha, *ACS Photonics* **2021**, *8*, 926.
- [44] H. Yu, Z. Zheng, Y. Mei, R. Xu, J. Liu, H. Yang, B. Zhang, T. Lu, H. Kuo, *Prog. Quantum Electron.* **2018**, *57*, 1.
- [45] S. Watson, S. Viola, G. Giuliano, S. P. Najda, P. Perlin, T. Suski, L. Marona, M. Leszczyński, P. Wisniewski, R. Czernecki, G. Targowski, M. A. Watson, H. White, D. Rowe, L. Laycock, A. E. Kelly, in *Advanced Free-Space Optical Communication Techniques and Applications II* (Eds.: L. Laycock, H.J. White), Proc. SPIE Vol. 9991, SPIE, Bellingham, WA **2016**, p. 99910A.
- [46] W. Chen, X. Wen, M. Latzel, M. Heilmann, J. Yang, X. Dai, S. Huang, S. Shrestha, R. Patterson, S. Christiansen, G. Conibeer, *ACS Appl. Mater. Interfaces* **2016**, *8*, 31887.
- [47] C. K. Sun, F. Vallée, S. Keller, J. E. Bowers, S. P. DenBaars, *Appl. Phys. Lett.* **1997**, *70*, 2004.
- [48] S. C. Kan, D. Vassilovski, T. C. Wu, K. Y. Lau, *Appl. Phys. Lett.* **1992**, *61*, 752.
- [49] P. W. M. Blom, C. Smit, J. E. M. Haverkort, J. H. Wolter, *Phys. Rev. B* **1993**, *47*, 2072.
- [50] R. Nagarajan, T. Fukushima, S. W. Corzine, J. E. Bowers, *Appl. Phys. Lett.* **1991**, *59*, 1835.
- [51] H. Yu, Z. Zheng, Y. Mei, R. Xu, J. Liu, H. Yang, B. Zhang, T. Lu, H. Kuo, *Progress in Quantum* **1993**, *29*, 1648.
- [52] S. C. Kan, D. Vassilovski, T. C. Wu, K. Y. Lau, *IEEE Photon. Technol. Lett.* **1992**, *4*, 428.
- [53] D. Saha, D. Basu, P. Bhattacharya, *Phys. Rev. B* **2010**, *82*, 205309.
- [54] D. Banerjee, R. Adari, M. Murthy, P. Suggiseti, S. Ganguly, D. Saha, *J. Appl. Phys.* **2011**, *109*, 07C317.
- [55] A. Othonos, *J. Appl. Phys.* **1998**, *83*, 1789.
- [56] J. Shah, *Ultrafast Spectroscopy of Semiconductors and Semiconductor Nanostructures*, Springer, Heidelberg **1999**.
- [57] J. D. Servaites, M. A. Ratner, T. J. Marks, *Energy Environ. Sci.* **2011**, *4*, 4410.
- [58] R. Berera, R. van Grondelle, J. T. M. Kennis, *Photosynth. Res.* **2009**, *101*, 105.
- [59] E. M. Grumstrup, M. M. Gabriel, E. E. M. Cating, E. M. Van Goethem, J. M. Papanikolas, *Chem. Phys.* **2015**, *458*, 30.
- [60] J. Cabanillas-Gonzalez, G. Grancini, G. Lanzani, *Adv. Mater.* **2011**, *23*, 5468.
- [61] Y. J. Yan, L. E. Fried, S. Mukamel, *J. Phys. Chem.* **1989**, *93*, 8149.
- [62] V. I. Klimov, *J. Phys. Chem. B* **2000**, *104*, 6112.
- [63] A. H. Zewail, *Angew. Chem., Int. Ed.* **2000**, *39*, 2586.
- [64] A. H. Zewail, *J. Phys. Chem. A* **2000**, *104*, 5660.
- [65] S. Chouksey, S. Sankaranarayanan, V. Pendem, P. K. Saha, S. Ganguly, D. Saha, *Nano Lett.* **2017**, *17*, 4596.
- [66] S. Chouksey, S. Sreenadh, S. Ganguly, D. Saha, *Nanotechnology* **2019**, *30*, 194003.
- [67] P. K. Saha, T. Aggarwal, A. Udai, V. Pendem, S. Ganguly, D. Saha, *ACS Photonics* **2020**, *7*, 2555.
- [68] P. K. Saha, V. Pendem, S. Chouksey, A. Udai, T. Aggarwal, S. Ganguly, D. Saha, *Nanotechnology* **2019**, *30*, 104001.
- [69] G. M. Christian, S. Schulz, M. J. Kappers, C. J. Humphreys, R. A. Oliver, P. Dawson, *Phys. Rev. B* **2018**, *98*, 155301.
- [70] S. Grosse, J. H. H. Sandmann, G. von Plessen, J. Feldmann, H. Lipsanen, M. Sopanen, J. Tulkki, J. Ahopelto, *Phys. Rev. B* **1997**, *55*, 4473.
- [71] P. D. Buckle, P. Dawson, S. A. Hall, X. Chen, M. J. Steer, D. J. Mowbray, M. S. Skolnick, M. Hopkinson, *J. Appl. Phys.* **1999**, *86*, 2555.
- [72] T. Aggarwal, S. Ganguly, D. Saha, *J. Phys. Chem. C* **2021**, *125*, 3535.
- [73] D. Nag, T. Aggarwal, R. Sarkar, S. Bhunia, S. Ganguly, D. Saha, A. Laha, *J. Opt. Soc. Am. B* **2019**, *36*, 616.
- [74] D. J. Colin Wood, *Polarization Effects in Semiconductors*, Springer US, Boston, MA **2008**.
- [75] L. H. Peng, C. W. Chuang, L. H. Lou, *Appl. Phys. Lett.* **1999**, *74*, 795.
- [76] V. Pendem, P. Saha, T. Aggarwal, S. Chouksey, A. Udai, S. Ganguly, D. Saha, in *OSA Advanced Photonics Congress (AP) 2019 (IPR, Networks, NOMA, SPPCom, PVLED)*, OSA, Washington, D.C. **2019**, p. PW3C.4.
- [77] S. Chouksey, P. K. Saha, V. Pendem, T. Aggarwal, A. Udai, S. Ganguly, D. Saha, *Appl. Surf. Sci.* **2020**, *518*, 146225.
- [78] J. P. Leburton, *J. Appl. Phys.* **1984**, *56*, 2850.
- [79] K. Park, A. Mohamed, M. Dutta, M. A. Stroschio, C. Bayram, *Sci. Rep.* **2018**, *8*, 15947.
- [80] I. Magnusdottir, A. V. Uskov, S. Bischoff, B. Tromborg, J. Mørk, *J. Appl. Phys.* **2002**, *92*, 5982.
- [81] A. S. Baltenkov, A. Z. Msezane, *Eur. Phys. J. D* **2016**, *70*, 81.
- [82] M. Asada, Y. Miyamoto, Y. Suematsu, *IEEE J. Quantum Electron.* **1986**, *22*, 1915.
- [83] J. H. Zheng, H. S. Tan, S. C. Ng, *J. Phys.: Condens. Matter* **1994**, *6*, 1695.
- [84] A. David, C. A. Hurni, N. G. Young, M. D. Craven, *Appl. Phys. Lett.* **2017**, *111*, 233501.